biomimetics

MDPI

Review

One Structure, Two Functions: Bioinspired Laser-Textured Photothermal Superhydrophobic Surfaces for Anti-/Deicing

Chunlei Gao [1,*], Yongyi Du [2] and Yongzhi Liu [3,*]

[1] School of Mechanical and Electrical Engineering, Taizhou Vocational and Technical College, Taizhou 318000, China
[2] School of Physics, Beijing Institute of Technology, Beijing 100081, China; 3120241564@bit.edu.cn
[3] School of Electronic and Information Engineering, Beijing Jiaotong University, Beijing 100044, China
* Correspondence: gaocl@tzvtc.edu.cn (C.G.); 25120297@bjtu.edu.cn (Y.L.)

Abstract

Ice accretion severely threatens the safety and operational efficiency of aircraft, wind turbines, and power-transmission facilities. Passive superhydrophobic surfaces can delay icing, yet they readily fail under low-temperature, high-humidity conditions. Coupling photothermal conversion with superhydrophobicity enables anti-icing through supercooled droplet repellency, interfacial ice melting, and meltwater drainage. This review surveys recent progress in laser-fabricated biomimetic photothermal superhydrophobic anti-icing surfaces. Hierarchical micro/nanostructures are identified as the shared structural basis that integrates broadband solar-light trapping with a stable Cassie–Baxter wetting state. Representative systems approach full-spectrum absorption and reduce ice adhesion by one to two orders of magnitude. Air-mass-1.5 (AM1.5)-weighted solar absorptance is adopted as the primary metric of photothermal performance. This paper compares femtosecond, picosecond, nanosecond, and continuous-wave laser routes, along with laser-induced graphene, in terms of mechanism, typical morphology, processing throughput, and performance limits. The paper examines discrepancies arising from inconsistent absorptance evaluation and ice-adhesion test protocols, and discusses the coupling among droplet repellency, ice-adhesion reduction, photothermal melting, and meltwater drainage. Finally, challenges in mechanical durability, all-weather reliability, scalable manufacturing, and characterization standardization are analyzed, and directions toward structurally integrated, low-energy-consumption anti-icing surfaces are outlined.

Keywords: biomimetic surfaces; laser texturing; superhydrophobic; photothermal anti-icing; hierarchical micro/nanostructures

Check for updates

Academic Editors: Stanislav N. Gorb and Jiaqi Miao

Received: 16 October 2026
Revised: 31 October 2026
Accepted: 1 November 2026
Published: 5 November 2026

Copyright: © 2026 by the authors. Licensee MDPI, Basel, Switzerland. This article is an open access article distributed under the terms and conditions of the Creative Commons Attribution (CC BY) license.

1. Introduction

Ice accretion is a common safety problem in aviation, wind power, power transmission, and transportation. Supercooled droplets freeze rapidly upon impacting wings, blades, and cables, degrading aerodynamic profiles, reducing energy-conversion efficiency, and threatening structural safety. Wing icing, for example, can cause fatal accidents in severe cases [1]; a single severe icing event at a cold-region wind farm can sharply reduce or even halt power output, and icing-related energy loss ranges from 0.005% to 50% of annual production [2].

All existing anti-/deicing strategies have limitations. Electrothermal heating is energy-intensive, pneumatic deicing boots disrupt the aerodynamic profile and increase fatigue

risk, and chemical deicing fluids raise pollution and maintenance concerns. Passive superhydrophobic surfaces (SHSs) inspired by lotus leaves [3] form a solid–liquid–air composite interface through surface topography and low-surface-energy chemistry. This composite interface reduces solid–liquid contact and promotes droplet shedding before freezing. However, the Cassie–Wenzel transition in cold, humid conditions, structural wear, and frost-induced internal nucleation can all cause purely passive anti-icing to fail.

Photothermal superhydrophobic surfaces, which combine superhydrophobicity with photothermal conversion, have therefore attracted attention. The superhydrophobic state repels supercooled droplets and delays nucleation; the photothermal effect melts interfacial ice into a lubricating water film that reduces ice adhesion, and the meltwater beads up and drains without refreezing. The micro/nanostructure simultaneously traps light and entraps air, providing the structural basis for integrating both functions on one surface. This passive–active integration requires illumination and remains vulnerable to mechanical wear and other structural failure modes.

Nature has long controlled light with micro/nanostructures: moth eyes suppress reflection through subwavelength papillae with a graded refractive index [4,5]; birds-of-paradise feathers reach 0.05–0.31% directional reflectance through tilted barbule arrays that form deep cavities [6]; and black butterfly wings hold visible reflectance below 0.4% through hierarchical scales [7]. Biomimetic design adopts these light-trapping principles rather than copying appearances. Laser processing reconstructs such geometries as microcones, deep cavities, and porous nanostructures [8], extending strong absorption across the main solar spectrum (250–2500 nm). More importantly, the same hierarchical roughness also entraps air to form a stable composite wetting state, so light trapping and superhydrophobicity share a structural homology. We use "bioinspired" in this restricted sense. The design principles, namely light-trapping geometries and air-entraining hierarchical roughness, are abstracted from the biological prototypes above. However, many of the laser-textured surfaces reviewed below were not developed by imitating a specific organism.

Homology, however, does not imply automatic synergy. Deep cavities and fine textures favor light trapping but may compromise Cassie-state stability. The two functions thus trade off in feature size, aspect ratio, and solid–liquid fraction. Reconciling them requires a unified design criterion. In this review, we call the design rationale that connects biological prototypes, structural physics, laser manufacturing, and anti-icing functions the "spectral-engineering bridge" (Figure 1). We use the term in a modest sense. It names an organizational framework for the review rather than a new physical mechanism or a new surface-treatment strategy, since the individual mechanisms are established. The framework adds the recognition that spectral response and wetting stability are governed by the same structural parameters and must therefore be co-designed.

Among artificial routes to such structures, laser micro/nanoprocessing stands out. Compared with lithography, etching, hydrothermal synthesis, or chemical deposition, it offers maskless direct writing and in situ generation of hierarchical structures [8]. It can build such dual-function structures on metals, ceramics, polymers, and composites. Crucially, laser processing reconstructs surface geometry and chemistry in a single energy-deposition step. Optical and wetting properties are thus co-regulated, providing the manufacturing basis of structural homology. This review covers only laser routes; non-laser methods such as templating, etching, spraying, and electrodeposition have been systematically reviewed elsewhere [9].

Existing reviews have established three foundations: theories of ice nucleation, growth, and adhesion [10,11]; laser-texturing control of surface micro/nanostructure, wetting behavior, and anti-icing performance [12–14]; and material systems, applications, and deicing mechanisms of photothermal superhydrophobic surfaces [15–18]. Each, however,

covers only one side of the problem. None has used laser manufacturing as the main thread to connect AM1.5-weighted solar absorptance and the full "repel–melt–drain" process, or to discuss weak-light compensation. This review fills this gap, with structural homology providing the physical basis and the "spectral-engineering bridge" providing the design framework. The discussion focuses on the representative literature since 2015, when foundational works in this area appeared, and tracks it through mid-2026.

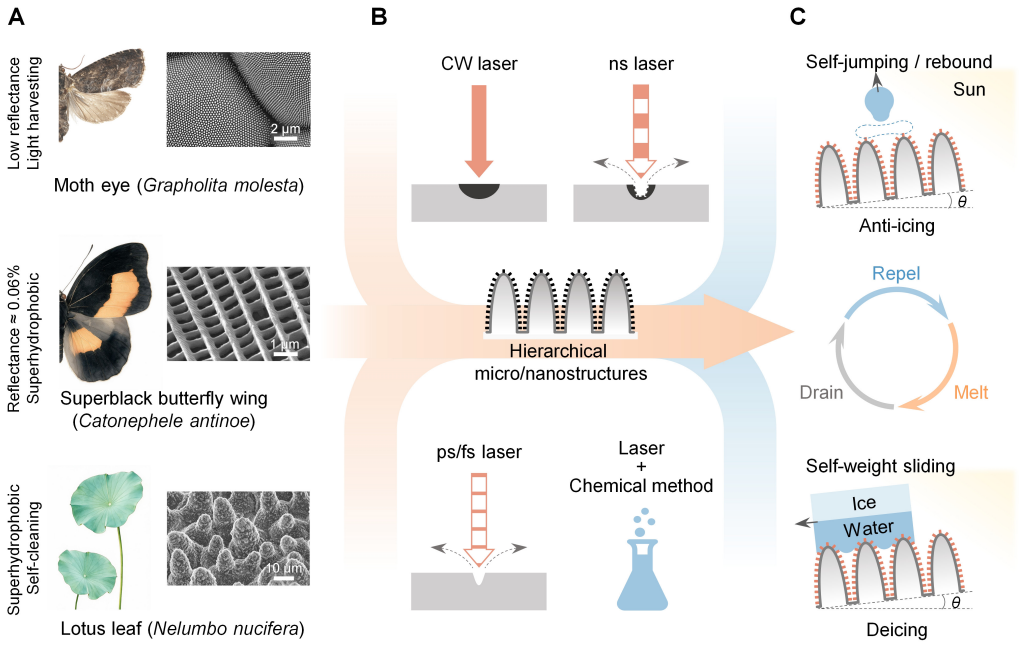

Figure 1. Bioinspired design concept of laser-fabricated photothermal superhydrophobic anti-/deicing surfaces. (**A**) Natural prototypes combining light harvesting and water repellency: the crepuscular moth compound eye (*Grapholita molesta*) with low-reflectance nipple arrays, the superblack butterfly wing (*Catonephele antinoe*, reflectance ≈ 0.06%), and the superhydrophobic, self-cleaning lotus leaf (*Nelumbo nucifera*). Scanning electron microscopy (SEM) images. Reproduced from Ensikat et al. [3], licensed under CC BY 2.0; Yang et al. [5], licensed under CC BY 4.0; Davis et al. [7], licensed under CC BY 4.0. (**B**) Laser fabrication routes (continuous-wave (CW), ns, ps/fs, and laser–chemical hybrid processing) reproducing the hierarchical micro/nanostructures shared by these biological prototypes. (**C**) These micro/nanostructures enable anti-icing and deicing through the "repel–melt–drain" cycle; the upper and lower schematics detail the anti-icing stage (droplet self-jumping/rebound) and the deicing stage (photothermal interfacial melting and self-weight ice sliding), respectively.

Figure 2 maps this development as a single timeline of laser-enabled milestones. Early milestones established the structural foundations: the laser-fabricated black surface (black silicon) in 1998 [19], the laser-fabricated superhydrophobic surface in 2006 [20], laser-superhydrophobic polymers [21] and metals [22] in 2008, aging-driven wettability control on patterned metals in 2009 [23], and laser-induced graphene from polymers in 2014 [24]. Laser-built anti-icing surfaces followed in 2015 [25], moth-eye-inspired photothermal anti-icing aluminum in 2021 [26], dual-energy-barrier structures for long icing delay [27] and wear-resistant multi-bioinspired icephobic microspine arrays [28] in 2024, and photothermal–wind synergistic deicing on superhydrophobic laser-induced graphene in 2025 [29], culminating in the metal–organic-framework (MOF)-armored [30] and angle-adaptive Janus [31] photothermal anti-icing systems of 2026. The review is organized as follows: Section 2 introduces the fundamentals of solar absorption, wetting, and photothermal conversion; Section 3 compares the four laser routes; Section 4 discusses passive

anti-icing, active deicing, and weak-light/no-light compensation; Section 5 analyzes durability, reliability, scalability, and characterization standardization; and Section 6 concludes.

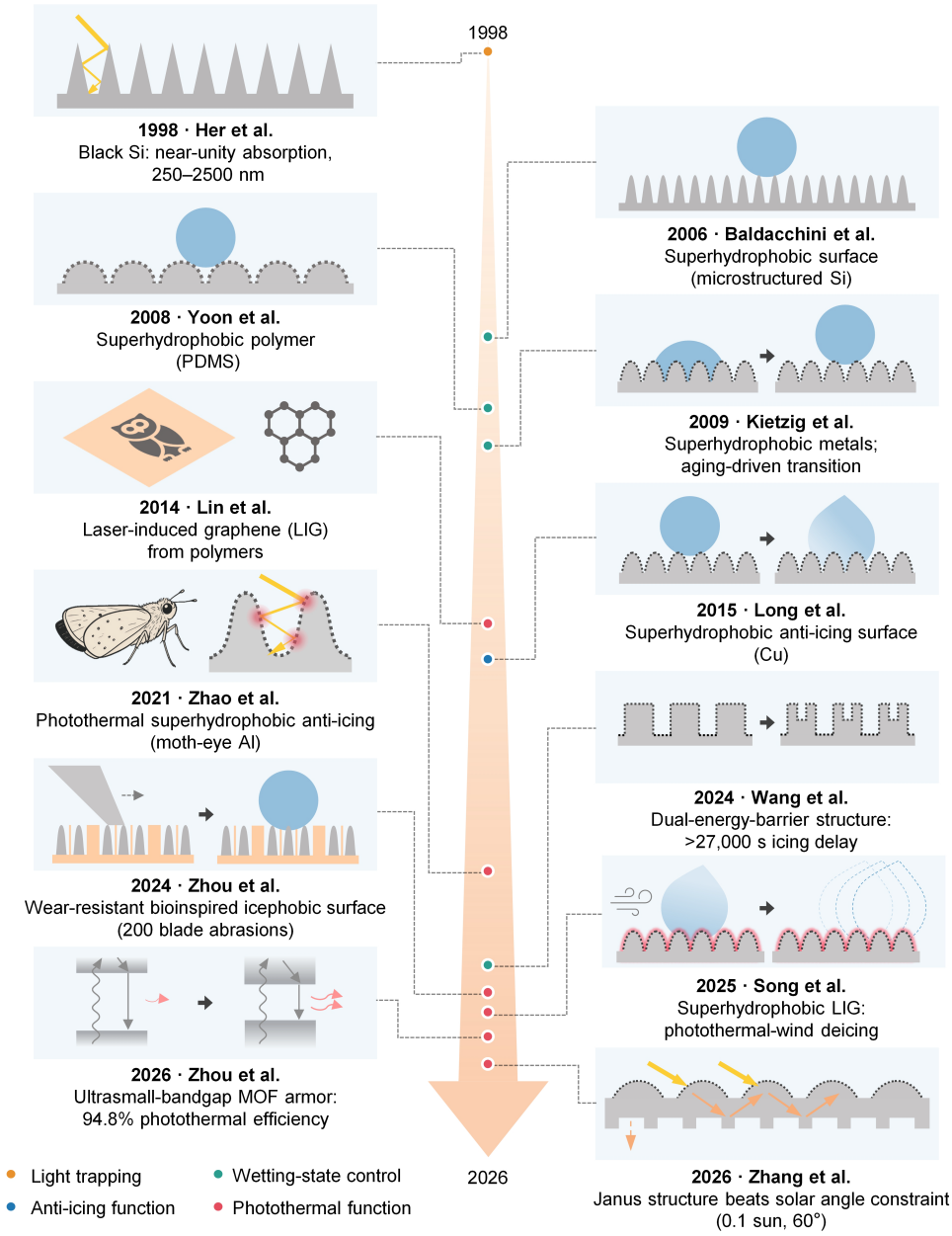

Figure 2. Development timeline of laser-fabricated superhydrophobic and photothermal anti-/deicing surfaces (1998–2026). Milestones progress from early light-trapping and superhydrophobic structures (1998–2014) [19–21,23,24] through the first laser-built anti-icing surfaces (2015–2021) [25,26] to integrated photothermal ice-protection systems (2024–2026) [27–31]. Colored markers on the timeline axis denote the primary enabling function(s) of each milestone: light trapping, wetting-state control, anti-icing function, or photothermal function. All icons are schematic redrawings rather than reproductions of the original figures.

2. Spectral Engineering Fundamentals

Designing photothermal superhydrophobic anti-icing surfaces involves three physical processes. This section discusses optical absorption, interfacial wetting, and photothermal conversion.

2.1. Solar Spectrum and Light-Trapping Mechanisms

The high absorption of laser-textured surfaces across the full spectrum results from several optical mechanisms. The AM1.5 standard solar spectrum is mainly distributed over 280–2500 nm. The ultraviolet (250–400 nm) accounts for about 5%, the visible (400–700 nm) for about 43%, and the near-infrared (700–2500 nm) for about 52%, while the energy at shorter wavelengths is negligible (ASTM G173-03(2020) [32]). Photothermal performance must therefore be measured by solar-spectrum-weighted absorptance over 250–2500 nm, where 250 nm is also the common lower limit of spectrophotometric measurement. The four mechanisms below all enhance absorption, but each applies to a different band (Figure 3).

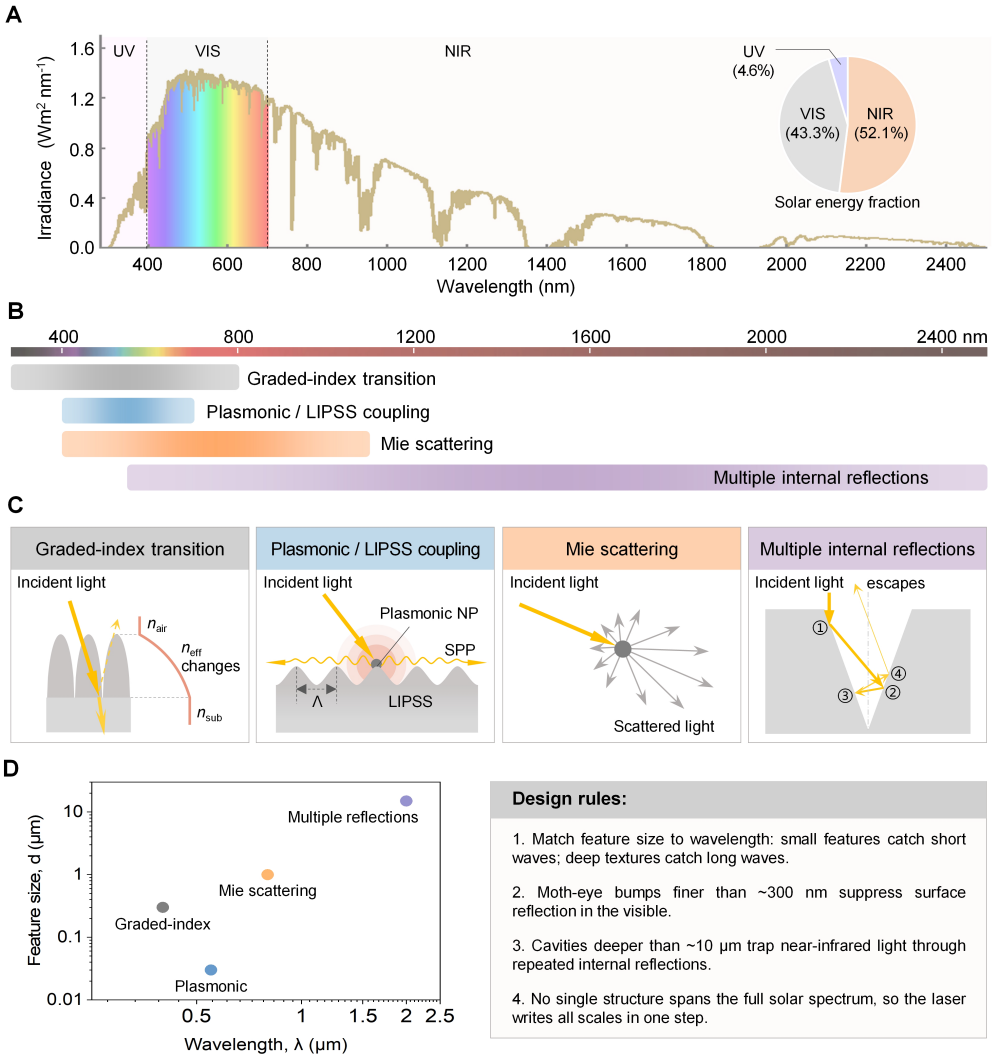

Figure 3. Solar spectral energy distribution and scale-matched light-trapping mechanisms of laser-textured surfaces. (**A**) AM1.5 solar irradiance spectrum (280–2500 nm) with the ultraviolet (UV), visible (VIS), and near-infrared (NIR) bands; the inset gives the solar energy fraction of each band. (**B**) Schematic spectral working windows of the four light-trapping mechanisms over 280–2500 nm. (**C**) Working principles of the four mechanisms, from left to right: tapered microcones grading the effective refractive index from air to substrate; plasmonic nanoparticles on LIPSS (period Λ) launching surface plasmon polaritons; wavelength-scale scatterers redirecting light via Mie scattering; and deep microcavities trapping light through multiple internal reflections. (**D**) Characteristic feature size versus operating wavelength for the four mechanisms (**left**) and the derived design rules for hierarchical laser texturing (**right**).

The first mechanism is multiple internal reflection (MIR), which mainly occurs in high-aspect-ratio microcone and micropillar structures [33,34]. Incident light reflects repeatedly

between the structure's sidewalls and is progressively absorbed. After N reflections, the structure's total absorptance satisfies:

$$\alpha_N = 1 - (1 - \alpha_0)^N \quad (1)$$

Here α_0 is the intrinsic single-bounce absorptance, a material property independent of geometry, whereas $\alpha_N = 1 - (1 - \alpha_0)^N$ is the structural total absorptance at a given wavelength and depends on the morphology. What ultimately determines photothermal performance is the AM1.5-weighted absorptance αsolar, the spectral average of $\alpha_N(\lambda)$ weighted by the AM1.5 irradiance (see Equation (6) in Section 2.3). For metals with $\alpha_0 \approx 0.5$, such as oxidized steel and titanium, about five internal reflections already push the total absorptance above 95%. Laser-textured cone arrays reach 99.3–99.35% over 300–2000 nm and remain above 98% even at 60° incidence [33,34].

The second mechanism is Mie scattering by dielectric scatterers. When oxide, ceramic, or polymer nanostructures are comparable in size to the incident wavelength, they scatter the light into a diffuse field within the surface layer. This extends the optical path and increases the material's probability of secondary absorption.

The third mechanism is the graded-refractive-index effect (moth-eye effect) [4]. Sub-wavelength textures smooth the refractive-index transition at the air–material interface and reduce Fresnel reflection. The effective medium approximation (EMA) describes this process. For a composite layer whose air fraction $f(z)$ varies with depth z, the effective refractive index is:

$$n_{eff}(z) = n_{air}^{f(z)} \cdot n_{material}^{1-f(z)} \quad (2)$$

Optimal broadband anti-reflection requires $f(z)$ to transition smoothly from one (pure air) at the surface to zero (bulk material), and laser-fabricated hierarchical structures often naturally approximate this ideal distribution. For example, femtosecond-laser-fabricated silicon moth-eye arrays (cone height at about 240 μm, period at about 67 μm) provide graded-index matching. After coating with a conformal pyrolytic carbon layer about 100 nm thick to supplement material absorption, absorption exceeded 98% over 1–1200 THz (300 μm–250 nm) [35].

The fourth mechanism is periodic-structure coupling and plasmonic absorption. When the period of laser-induced periodic surface structures (LIPSSs) matches the incident wavelength, the periodic ripples act as a diffraction grating, providing wave-vector matching and exciting surface plasmon polaritons. Metal nanoparticles can also localize energy and dissipate it as heat through localized surface plasmon resonance (LSPR).

Each mechanism operates over a characteristic spectral band. Microscale cone arrays trap the visible and short-wave near-infrared but lose efficiency at longer wavelengths [34]. Nanoscale scatterers act weakly at long wavelengths; the bandwidth of a graded-index layer is limited by the texture depth [35]. A solar-spectrum photothermal surface therefore requires combining microscale and nanoscale structures, with "structure–wavelength matching" as the design benchmark. This criterion also holds in biological prototypes. Ultrablack butterfly wings combine ridges, crossbeams, and nanoscale holes to suppress the reflectance to 0.06–0.4% at 500 nm within a micron-scale thickness. Removing the ridges or crossbeams raises the reflectance by a factor of 3–16 in optical simulations [7].

2.2. Wetting Behavior of Laser-Textured Surfaces

The wetting characteristics of laser-textured surfaces depend on both surface topography and surface chemistry. The classical Young, Wenzel, and Cassie–Baxter models describe, respectively, an ideally smooth surface, a fully wetted rough surface, and a composite sur-

face with entrapped air. Together they form the basis for analyzing superhydrophobic anti-icing interfaces.

The Young model [36] gives the intrinsic equilibrium contact angle of an ideally smooth surface.

$$cos\theta_Y = (\gamma_{SV} - \gamma_{SL})/\gamma_{LV} \quad (3)$$

The Wenzel model [37] describes the fully wetted state in which liquid completely impregnates the rough structure. The roughness factor r amplifies the material's intrinsic wettability, and the apparent contact angle satisfies:

$$cos\theta_W = rcos\theta_Y \quad (4)$$

The Cassie–Baxter model [38] describes the composite wetting state in which a droplet rests on the structure peaks with air trapped in the gaps. Its apparent contact angle satisfies:

$$cos\theta_{CB} = f_{SL} \cdot (cos\theta_Y + 1) - 1 \quad (5)$$

Here, f_{SL} is the solid–liquid contact area fraction. When hierarchical multiscale roughness reduces f_{SL} below 0.05, the apparent contact angle estimated by Equation (5) exceeds 150°, entering the superhydrophobic regime.

Anti-icing performance depends more directly on fracture and sliding at the ice–solid interface. Ice adhesion on smooth metal surfaces typically ranges from several hundred kPa to 1 MPa. A stable air layer reduces solid–ice contact, allowing cracks to initiate and propagate in the air gaps, and can reduce ice adhesion to about 1.6 kPa [39], approaching the interfacial limit of an "air-cushion separation." Mushroom-like cross-scale structures further combine re-entrant overhangs with a pressure-resistant design, exhibiting a contact angle above 167° and ice adhesion as low as 0.46 kPa, remaining below 5 kPa after 15 deicing cycles [40].

The wettability of laser-textured surfaces also evolves with aging. Freshly ablated metals are superhydrophilic (contact angle < 10°) because of oxidation and polar-group formation, and gradually become hydrophobic or superhydrophobic upon air exposure [41,42]. X-ray photoelectron spectroscopy (XPS) analyses show that the surface carbon content increases gradually during storage, and the steady-state contact angle correlates positively with the carbon content. This transition has been attributed to slow CO_2 decomposition on the surface and the accumulation of nonpolar carbon [23]. Studies on laser-processed copper also indicate that adsorption of atmospheric light hydrocarbons can drive this transition [43]. Although natural aging can reduce the need for modification steps, low-surface-energy modification with fluorosilanes remains the mainstream method for accelerating and stabilizing the superhydrophobic state.

2.3. Structure-Enhanced Photothermal Conversion

Photothermal conversion on a laser-textured surface is a cascaded energy-transfer process. In metals, photons are first absorbed via free-electron excitation, then converted to lattice heat through electron–phonon coupling [44], and finally diffuse toward the substrate and the environment. At the material level, the energy-dissipation pathways mainly include plasmon damping, non-radiative relaxation in semiconductors, and molecular thermal vibration in carbon-based and conjugated systems. These pathways determine how efficiently absorbed photon energy is converted to heat, whereas the structural light-trapping mechanisms in Section 2.1 determine how much incident light enters the conversion pro-

cess. The steady-state temperature rise is determined by the balance between the absorbed power and the convective and radiative dissipation.

$$\Delta T = \alpha \cdot I \cdot A_{surface} / \left(h \cdot A_{contact} + \varepsilon \cdot \sigma \cdot A_{surface} \cdot 4T_0^3 \right) \quad (6)$$

Here α is the surface absorptance, I the incident irradiance, A_{surface} and A_{contact} the illuminated area and the convective heat-transfer area, h the convective heat-transfer coefficient, ε the emissivity, σ the Stefan–Boltzmann constant, and T_0 the ambient temperature. Three clarifications are necessary regarding the symbols in Equation (6). First, α is the AM1.5-weighted solar absorptance αsolar, the AM1.5-irradiance-weighted spectral average of the structural absorptance $\alpha_N(\lambda)$ in Equation (1) (Section 2.1). Using the intrinsic absorptance α_0 or any single-wavelength value in its place overestimates the photothermal capability. Second, Equation (6) assumes steady state, a uniform surface temperature, constant h and ε, and negligible substrate conduction. Its radiative coefficient $4\varepsilon\sigma{T_0}^3$ follows from $\varepsilon\sigma(T^4 - {T_0}^4) \approx 4\varepsilon\sigma{T_0}^3\Delta T$ for $\Delta T \ll T_0$ and is thus valid for one-sun anti-icing tests but not high-temperature solar-thermal applications. Third, ε governs radiative heat loss. A low ε suppresses radiation in high-temperature applications, whereas near-room temperature radiative loss is secondary to convection. Even so, ε is always reported with the absorptance (Section 5.4).

Equation (6) shows that the steady-state temperature rise increases mainly because of higher absorptance α, which results directly from the structural light trapping discussed in Section 2.1. Under comparable heat-dissipation conditions, a laser-textured surface has a higher steady-state temperature rise than bare metal. In addition, absorption and heat generation are concentrated in the surface micro/nanostructures, so heat is released near the ice–substrate interface and spreads laterally through the surface layer beyond the illuminated spot, helping enlarge the effective deicing area.

2.4. Effects of Processing Parameters

Laser processing parameters regulate structure and performance. Pulse width determines processing precision and access to nanostructures. Fluence and pulse number control aspect ratio and morphological evolution. Scanning strategy and processing atmosphere adjust structural distribution and chemical composition. Together, they determine whether hierarchical roughness can simultaneously support full-spectrum absorption and a stable Cassie–Baxter state.

The pulse width determines the structural hierarchy. Nanosecond lasers produce a large heat-affected zone and mainly form microcones. Picosecond lasers can preserve nanoaggregates and submicron ripples. Femtosecond lasers directly form subwavelength structures such as LIPSS through "cold ablation". Shorter pulses generally yield richer nanostructures and greater potential to improve light absorption and hydrophobicity simultaneously.

The fluence and pulse number control the aspect ratio and morphological evolution. Moderate fluence favors regular, high-aspect-ratio microcones that simultaneously support multiple internal reflections and air entrapment, whereas excessive fluence causes molten collapse and weakens both functions. Increasing the pulse number generally drives the morphology from protruding to recessed.

The scanning path, geometric design, and atmosphere play secondary regulatory roles. The scanning path affects air-pocket connectivity. Unidirectional line scanning forms interconnected open grooves, whereas closed-grid scanning forms closed air cells separated by frames [45]. Re-entrant structures [39] and cross-scale hierarchical structures [46] can enhance pinning of the three-phase contact line and the stability of the air layer, respectively; Section 4.1 discusses their effects on ice adhesion and icing delay. For example, a honeycomb-inspired hexagonal protective frame can share the load for the cactus-spine-like

microspines inside it, reducing the maximum stress on the microspines by about two-thirds. The surface retains a superhydrophobic state with a contact angle of about 150.7° and a sliding angle of about 10.3° after 200 cycles of linear blade abrasion [28]. The processing atmosphere can enhance intrinsic absorption through in situ oxidation, whereas fluorosilane modification lowers surface energy based on existing nanoscale topography.

Structural homology does not hold across all structural parameters. At excessively large aspect ratios, condensed microdroplets fill the structure, and droplet impact more readily induces Cassie-state failure, while the structure's mechanical fragility rises simultaneously. Most reports of "enhanced photothermal performance accompanied by degraded hydrophobicity" originate from this regime. Divergent conclusions in the literature therefore often reflect different aspect-ratio windows and test conditions rather than a conflict at the principle level. Within a moderate window, light trapping and superhydrophobicity are enhanced in the same direction (see Section 4.2). For example, a cone-array ultrablack surface achieves an average absorptance of 99.35% over 300–2000 nm while exhibiting a contact angle of about 150° and a sliding angle of about 8° [33]. This shows that efficient light trapping and water repellency can coexist on the same hierarchical structure. This is precisely the observable and designable basis of the "spectral-engineering bridge".

3. Laser Manufacturing Strategies

Laser fabrication of photothermal superhydrophobic surfaces covers femtosecond, picosecond, nanosecond, and continuous-wave routes. Their essential differences stem from the energy-deposition timescale, and Figure 4 maps this origin-to-outcome chain in three layers. At the single-pulse level (Figure 4A), photon energy is first deposited into the electronic system within fs–ps: through free-electron generation by multiphoton and avalanche ionization in semiconductors and dielectrics, and through direct laser–electron heating in metals [47,48]. The excited material then follows non-equilibrium phase-transformation pathways over ps–10^2 ps (plasma formation, Coulomb explosion [49], and nonthermal melting in semiconductors and dielectrics, versus competing homogeneous and heterogeneous melting in metals), before ablation, melt flow, and resolidification set the final morphology over 10^2 ps–10^2 ns [47,48,50].

These paths shift systematically with pulse width and fluence. As pulse width increases, peak power decreases and heat accumulation intensifies, and the dominant regime evolves from femtosecond non-equilibrium cold ablation, through picosecond mixed thermal–nonthermal ablation [51–53] and nanosecond thermally confined ablation, to continuous-wave melt–Marangoni convection and photothermal pyrolysis of laser-induced graphene [54]. Figure 4B condenses the coupled cost of this shift into two master curves: machining quality degrades while the heat-affected zone and recast extent grow as the regime turns thermal. The accumulated pulse number N then provides a second, orthogonal control knob (Figure 4C): through incubation, the effective ablation threshold decreases as $F\mathrm{th}(N) = F\mathrm{th}(1)\cdot N^{S-1}$, and features coarsen from nanoscale ripples through sub-microstructures to microscale textures while the surface reflectance falls accordingly. The corresponding manufacturing capability likewise shifts from nanoscale precision toward industrial throughput and material–chemistry conversion. Laser selection is thus, in essence, a trade-off among structural scale, photothermal performance, and manufacturing throughput. Section 3.6 provides a quantitative comparison.

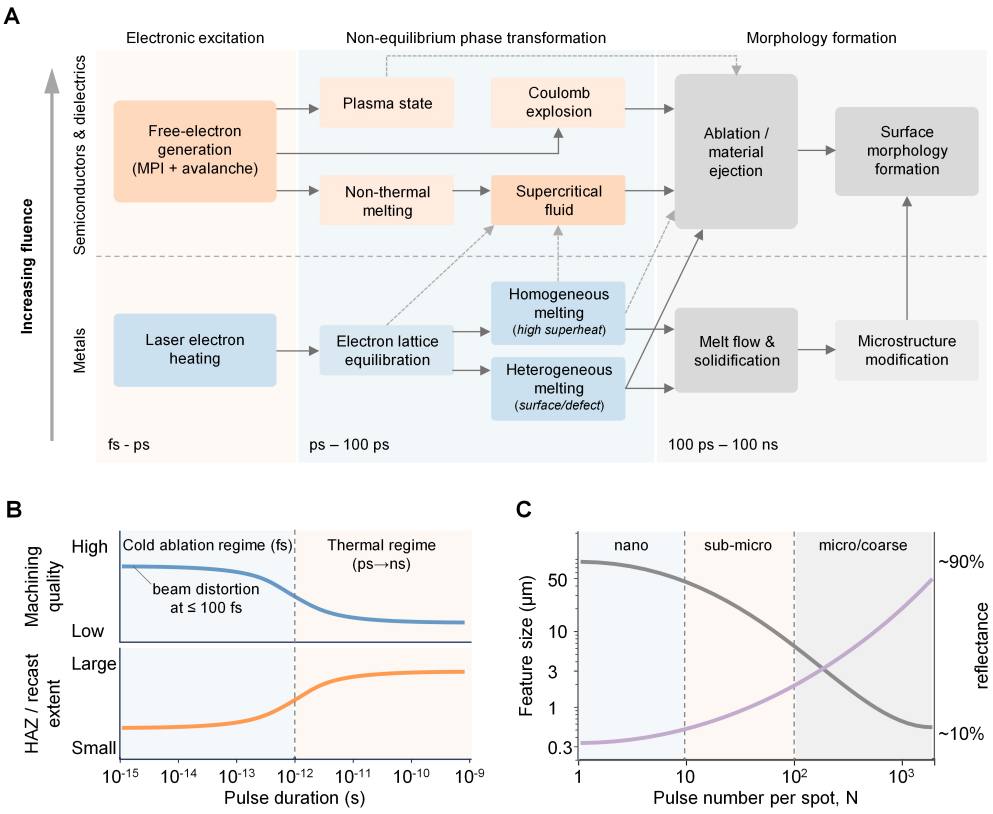

Figure 4. Timescale physics of laser surface texturing. (**A**) Single-pulse laser–matter interaction pathways for semiconductors/dielectrics (orange) and metals (blue) across three stages: electronic excitation (fs–ps), non-equilibrium phase transformation (ps–100 ps), and morphology formation (100 ps–100 ns), redrawn and adapted from Wang et al. [55], licensed under CC BY 4.0. (**B**) Machining quality and heat-affected-zone/recast extent versus pulse duration, contrasting the cold-ablation (fs) and thermal (ps–ns) regimes. (**C**) Feature-size growth and reflectance decay with accumulated pulse number per spot N [56,57]; shaded bands mark the nano-, sub-micro-, and micro-/coarse structure regimes.

3.1. Femtosecond Lasers

The femtosecond (fs) laser pulse width (10^{-15} s) is shorter than the electron–phonon coupling time, enabling "cold ablation" with a minimal heat-affected zone and submicron-resolution processing. Its peak intensity of 10^{12}–10^{15} W/cm^2 can also excite multiphoton ionization and avalanche breakdown, generating free electrons directly inside the material, so even weakly absorbing or transparent materials can be processed.

LIPSSs are the signature structures of femtosecond lasers. They appear as parallel ripples with a period close to the laser wavelength, arising from interference between the incident light and waves scattered off the surface. Adjusting the fluence yields low-spatial-frequency LIPSS (period ≈ wavelength) or high-spatial-frequency LIPSS (period ≈ half-wavelength). Their subwavelength period can enhance absorption through grating coupling. In scale, they also resemble the subwavelength anti-reflective papillae of moth eyes and can be regarded as laser-in situ-generated moth-eye-like textures. For example, a moth-eye-inspired textured aluminum surface exhibits a contact angle of 162°, a sliding angle as low as 3°, absorptance above 90% over 200–1100 nm, and a temperature rise from about 35 °C to about 83 °C within 300 s under one sun [26].

Beyond LIPSS, femtosecond lasers can also fabricate microgrooves, micropillars, and micropits [58]. At moderate-to-low fluence and high pulse number, a three-level structure of "microcones, submicron ripples, and nanoparticles" can form [59–61], simultaneously enhancing multiple internal reflections, plasmonic absorption, and air entrapment. Exper-

imentally, femtosecond-laser-blackened Au, W, and titanium alloys reach absorptances of 85–95% over 250–2500 nm [59]. Femtosecond-textured aluminum, titanium, and steel surfaces composited with silver nanoparticles reach solar-spectrum absorptances of 97.2%, 98.3%, and 98.9%, respectively [62]. A stainless-steel surface combining microcones with oxide nanospikes shows an average reflectance of about 0.96% over 250–2000 nm together with a water contact angle of about 156° [61]. Such near-blackbody surfaces retain high emissivity for 150 h at 1000 °C even in ambient air [63].

Femtosecond lasers can also process non-metallic substrates, such as polytetrafluoroethylene (PTFE) and polydimethylsiloxane (PDMS), and ceramics such as silicon carbide and zirconia. For example, one-step femtosecond direct writing on polyether ether ketone (PEEK) yields a superhydrophobic photothermal surface. The contact angle reaches about 161°, the absorptance about 94.6%, and the one-sun temperature rise is 44.5 °C [29]. During femtosecond scanning of silicone rubber, in situ deposition of ablation ash likewise forms micro/nanocomposite structures [64]. However, scanning speeds are usually only millimeters to tens of millimeters per second, and equipment costs are high. Ablation debris also tends to redeposit on the surface, often requiring post-cleaning. Laser-plasma-shockwave-assisted cleaning can eliminate this redeposition, enabling uniform black silicon over 50 mm × 50 mm with an average absorptance of 99.15% across 0.3–2.5 μm [65]. To overcome throughput limits, femtosecond lasers can fabricate durable master molds, whose structures are then replicated onto polymers by hot embossing or casting. A tungsten-carbide mold retained a contact angle above 150° after more than twenty consecutive hot-embossing cycles on polypropylene [66]. Similar routes have produced anti-icing PDMS and silicone-rubber/carbon-nanotube surfaces [67,68].

The femtosecond route offers the finest and most material-universal structuring, but throughput and cost remain bottlenecks. Mold replication bypasses the throughput limit but transfers only geometry, not in situ oxide chemistry. As a result, replicas usually show weaker optical performance than the laser-processed master. Femtosecond processing is therefore best regarded as a precision tool for high-value components and mold fabrication rather than a general-purpose large-area method.

3.2. Picosecond Lasers

The picosecond (ps) pulse width (10^{-12} s) is close to the electron–phonon coupling time. The heat-affected zone is larger than in femtosecond processing but much smaller than in nanosecond processing, and the precision and throughput fall between the two, making this route suitable for fabricating full-spectrum absorbing surfaces. Compared with nanosecond processing, picosecond pulses confine the energy deposition to the surface layer and suppress heat diffusion into the bulk [51]. Picosecond-laser-interference patterning can produce periodic microstructures on metal molds at high throughput and, combined with hot embossing, further amplifies this throughput advantage [53].

Picosecond lasers can fabricate coral-like porous structures on copper, composed of micron-scale skeletons, nano-aggregates, and submicron ripples. Such structures reach a peak visible absorptance of 97% and an average absorptance above 90% over 250–2500 nm [69]. Their multiple internal reflection and scattering paths resemble the melanin-rod arrays of bird-of-paradise feathers, illustrating that biomimetic multilevel scattering structures can broaden the solar absorption band. The processing speed of tens of millimeters per second also offers industrial potential.

On titanium and its alloys, picosecond processing can form composite structures of micropits and nanoripples. Picosecond-laser-interference-textured Ti6Al4V surfaces modified with perfluoropolyether reach a contact angle of about 163° and a sliding angle of about 8°, and retain their hierarchical structure and superhydrophobicity after 16 icing–

deicing cycles [70]. These titanium alloys are common materials for aircraft skins and engine components, and the high contact angle and low sliding angle favor shedding supercooled droplets before freezing, making this route suitable for aerospace anti-icing. On various metallic substrates, picosecond texturing combined with low-surface-energy modification yields superhydrophobicity. Nickel–aluminum bronze exceeds 150° [71], and 7075 aluminum alloy reaches 154° [72]. An FH40 cryogenic-steel surface reaches a contact angle of 160.5° and a sliding angle of about 1°, with an icing delay of 1935 s at −10 °C (about 60 times that of the untreated surface) and an ice-adhesion strength as low as about 45 kPa [52].

The picosecond route balances precision and throughput, but this balance is also its weakness. It inherits a non-negligible heat-affected zone from the nanosecond side, so its nanoscale roughness and the resulting Cassie stability are inferior to femtosecond structures, while its cost and throughput remain far from nanosecond levels. Much of the picosecond literature reports either optical or wetting properties alone, and studies that report full-spectrum absorptance, wettability, and one-sun temperature rise on the same sample are still scarce (see Section 3.6). Quantitative cross-route comparisons therefore remain difficult. The route is most justified where nanosecond quality is insufficient, but femtosecond throughput is unaffordable.

3.3. Nanosecond Lasers

The nanosecond (ns) pulse width (10^{-9} s) is much longer than the electron–phonon coupling time of metals, so thermal diffusion and a molten layer are significant, and the minimum feature size is limited. However, its high throughput and low cost make it suitable for large-area industrial applications.

On stainless steel, aluminum, and copper, 1064 nm nanosecond fiber lasers can directly form microcone arrays through cumulative ablation and capillary melt redistribution [42,73], without templates or polymer reshaping. A moderate fluence favors regular cones, whereas excessive fluence produces irregular cones or craters. These structures function similarly to the cavity arrays of black papilionid butterfly wings by extending the optical path and trapping air, and the oxide layer formed during air processing can further enhance ultraviolet–visible absorption. Nanosecond-fiber-laser-textured black-silicon surfaces reduce the reflectance to below 14.3% over 300–1200 nm [74].

Nanosecond-textured metals can likewise support photothermal anti-icing. Ultraviolet-laser-marked stainless-steel microgrooves with a titanium nitride@silica (TiN@SiO_2) armor layer exhibit a contact angle of about 160° and a one-sun temperature rise of about 35 °C [75]. Laser-engraved mosquito-eye-inspired copper microspike arrays with candle-soot deposition reach a contact angle of 154.9° and a one-sun temperature rise of 45.2 °C [76]. However, the limited nanoscale roughness weakens Cassie stability under dynamic impact and condensation compared with ultrafast-laser structures. Re-entrant structures further enhance the Cassie robustness. A nanosecond-textured re-entrant metal surface shows an icing delay exceeding 600 min and an ice-adhesion strength as low as 1.6 kPa. The adhesion remains below 25 kPa after 100 deicing cycles [39]. In addition, one-step nanosecond processing of carbon-fiber-reinforced polymers (CFRPs) reaches a contact angle of about 161° [77], extending the route from metals to aerospace composites.

The nanosecond route is the most mature for industrialization, but its thermal-confinement nature sets a hard floor on structural fineness. The attainable nanoscale roughness is limited, so superhydrophobicity relies more on chemical modification and aging (see Sections 2.2 and 3.5). High absorptance also depends on the in situ oxide layer, and long-term outdoor oxidation or contamination may cause optical performance to drift. Re-entrant geometries restore the Cassie robustness, but their overhangs are fragile and

slow to fabricate, partially offsetting the throughput advantage. Nanosecond processing is thus the pragmatic choice for large-area metal surfaces with moderate performance targets, not the route to the highest optical or wetting performance.

3.4. Continuous-Wave Lasers

Continuous-wave (CW) lasers are dominated by sustained heat input. They cannot form subwavelength structures such as LIPSSs, which rely on non-equilibrium processes. Instead, they provide industrial throughput for large-area melting-based texturing and drive photothermal–chemical conversions such as laser-induced graphene (LIG).

Continuous-wave CO_2 laser induction of graphene is a photothermal–chemical modification. It locally heats a carbon-containing substrate above 2500 °C, driving deoxygenation, graphitization, and gas release to form a highly porous, electrically conductive three-dimensional graphene network [24]. However, LIG formation requires a carbon-rich precursor, which bare metals such as steel, aluminum, copper, and titanium lack. To obtain LIG on metal components, one must first introduce a carbon source, and three practical routes exist. The metal can be coated or laminated with a polymer precursor film, as in the polyimide-on-aluminum (PI@Al) scheme, in which the CO_2 laser converts only the polymer layer while the metal serves as a structural support and heat spreader [78]. Precursor solutions such as lignin, phenolic resins, or polyimide inks can instead be sprayed or cast before lasing, or LIG can be fabricated on a polymer substrate and transferred onto the target surface. Each route adds an interface whose adhesion and thermal contact govern durability, so claims of "metal compatible LIG" should be read with this interfacial complexity in mind.

3.4.1. Laser-Induced Graphene

Continuous-wave CO_2 lasers (10.6 μm) produce LIG through strong long-wave infrared absorption and transient high-temperature pyrolysis, giving high yield and well-developed porosity. Pulsed ultraviolet or ultrafast lasers improve the spatial resolution but rely mainly on photochemical dissociation and give lower yields. For example, femtosecond lasers construct multifunctional LIG in situ on arbitrary substrates such as paper, with an absorptance of about 98.8% and a contact angle of about 153.4° [79]. The contrast between the two routes shows that the laser's energy-deposition mode directly determines the material-conversion pathway.

The porous LIG network absorbs strongly across the ultraviolet–visible–near-infrared (UV–Vis–NIR) range through interband transitions and free-carrier absorption. Its conductivity additionally supports Joule heating, enabling photothermal/electrothermal dual-mode systems that overcome the failure of purely photothermal schemes in dark environments [80]. Femtosecond lasers also synthesize high-entropy-alloy nanoparticles in situ on LIG surfaces, enhancing the Joule-heating performance [81]. Polymer-derived LIG is moreover flexible, suiting curved and wearable components [82].

CO_2-laser-written hydrophobic LIG line arrays delay droplet freezing and, via Joule heating, deice rapidly without light. The surface temperature rises to 100 °C within 15 s [54]. Fluorinated LIG coatings reach a contact angle of 161.2° and a sliding angle of about 1.6°, extending the icing delay from 106 s to 868 s at −15 °C. Combining a superhydrophobic LIG layer with an electrothermal layer saves 48.75% of the energy in static environments and 17.4% in dynamic environments compared with purely electrical heating [83]. Ni decoration adds a magnetothermal pathway to LIG deicing [84]. A Ni-decorated LIG hierarchical surface reaches a contact angle of 162.6° and an icing delay of 224.8 s. It deices within 63.2 s under illumination, 56.2 s under electrical input, and 83.0 s under a magnetic field. However, the fluorination step behind the superhydrophobicity conflicts

with the growing fluorine-free regulatory trend (see Section 5.5). The porous network also wears easily and then loses conductivity and water repellency together, so the dual-mode advantage degrades faster than the bulk material wears. Femtosecond-laser-induced atomic-scale restructuring of LIG offers a new route to regulate its photothermal and electrical properties [85].

3.4.2. Surface Melting

Continuous-wave laser surface melting redistributes the melt through Marangoni convection, forming micron-scale ripples, microgrooves, and humps after solidification. For metals, these melted textures lack nanoscale roughness. Their fresh surfaces are usually superhydrophilic and require aging or chemical modification. Their Cassie stability is weaker than in ultrafast-laser structures, and their full-spectrum absorption relies on in situ oxidation.

The absence of nanoscale roughness depends on the substrate. On pyrolyzable polymers such as PDMS, continuous-wave lasers deposit SiO_2 nanoparticles in situ through pyrolysis–oxidation, superimposing nanoscale clusters on the micron-scale morphology to form a micro/nanohierarchy [86]. One-step laser melting of a PDMS/carbon-black membrane onto woven stainless-steel wires assembles coral-shaped micro/nanostructures on a submillimeter wire frame [87]. The surface reaches a contact angle of 160° and an ice adhesion of 14.5 kPa, and it deices within 123 s under one sun in frozen rain. It maintains a rolling angle below 10° after 538 m of ASTM D4060 abrasion. A 4200 cm^2 area was fabricated within 2 h. The core advantage of this route is industrial maturity. Kilowatt-class continuous-wave fiber lasers are already standard equipment for cutting and welding, and scan at meters per second, fast enough for large-area processing.

3.4.3. Secondary Treatment

Continuous-wave or low-energy pulsed lasers can also serve as a post-treatment. Secondary heat treatment of a textured surface adjusts the phase ratio of copper oxides, enhances the intrinsic absorption, and accelerates surface-energy reduction and air aging. This route uses no fluorinated reagents and aligns with green manufacturing (see Section 5.5).

The continuous-wave route trades structural precision for throughput and materials chemistry. LIG circumvents the precision limit by converting matter rather than shaping it, but ties the process to carbon-rich precursors. Continuous-wave processing is therefore best positioned as an industrial large-area texturing tool with moderate performance targets, or as a conversion tool for carbon precursors, rather than as a route to high-quality hierarchical textures on metals.

3.5. Laser–Chemical Synergy

Single-step laser texturing has a performance ceiling. Hybrid strategies that combine laser structuring with chemical/material modification can further raise performance [88–90].

The first category is laser-assisted surface-chemistry regulation. Adjusting the processing atmosphere (air, oxygen, or humidified gas) can generate metal-oxide layers in situ during ablation, whose interband transitions enhance intrinsic absorption. Section 3.4 discusses specific phase regulation.

The second category is laser-assisted loading of photothermal materials. Researchers can pre-coat a metal surface with graphene oxide (GO) and laser-reduce it to reduced graphene oxide (rGO). GO contains many oxygenated groups that disrupt the conjugated network, limiting its intrinsic absorption and conductivity. Laser reduction removes these groups and restores the sp^2-conjugated structure, providing broadband optical absorption and the conductivity required for Joule heating [91,92]. Laser-induced forward transfer (LIFT) can pattern and transfer donor metal films onto acceptor surfaces [93,94], enabling

the loading of Au, Ag, and other plasmonic particles. Table 1 summarizes the typical photothermal material systems, mechanisms, and representative performance.

Table 1. Typical photothermal material systems integrable with laser processing. Mechanisms and representative performance.

Material System	Dominant Photothermal Mechanism and Effective Band	Representative Performance and Laser Integration	Inherent Limitations
Porous carbon, LIG/rGO	Interband transitions and free-carrier absorption; full UV–NIR	Hydrophobic LIG line arrays delay icing and allow Joule deicing (100 °C within 15 s) [54]	Porous network is mechanically fragile; LIG is restricted to carbon-rich precursors (no direct formation on bare metals)
Transition-metal nitrides (TiN/ZrN)	Metallic free-carrier/plasmonic absorption; visible–NIR	High-temperature and oxidation-resistant, suitable for laser-composite coatings; laser microgrooves with a TiN@SiO_2 armor reach a contact angle (CA) of ≈160° and a 1-sun ΔT of ≈35 °C [75]	Ceramic layers are brittle; plasmonic absorption is band-limited and thickness-sensitive
Conjugated polymers (e.g., polydopamine, PDA)	Molecular thermal vibration and non-radiative relaxation; UV–NIR	Can be deposited in combination with laser-textured layers	Limited thermal and UV stability; film thickness hard to control
MXene and its composites	Free-carrier absorption and interlayer multiple scattering; UV–NIR	Photothermal/electrothermal dual-mode compatible; suitable for laser-patterned compositing	Prone to oxidation in humid air; nanosheet restacking reduces the accessible area
MOF-derived carbon/metal composite layers	Porous scattering, interband transitions, and interfacial loss; spectrally tunable	A honeycomb-skeleton-supported narrow-bandgap MOF reaches a photothermal conversion efficiency of 94.79% [30]; a Cu-MOF whisker surface shows absorptance > 98% and a 1-sun temperature rise of 65.5 °C [95]	Multi-step synthesis; framework may collapse under wear
Au/Ag plasmonic nanoparticles	LSPR absorption; tunable in visible–NIR	Can be pattern-loaded by LIFT [93]; enhances local absorption but cost must be evaluated	LSPR absorption is narrowband; noble-metal cost is high; particles may detach or coarsen

Note: The test irradiance, spectral band, and environmental conditions differ among the material systems. The values in this table indicate orders of magnitude only and must not be compared across rows without normalization. Any quantitative cross-comparison presupposes the standardized reporting protocol of Section 5.4.

The third category adds external nanostructures to laser-textured surfaces. Nanowires or nanosheets can be grown hydrothermally on laser-processed microstructures, and nanoparticle coatings such as carbon nanotubes and SiO_2 can be sprayed or deposited. Both routes supply the missing nanoscale roughness and introduce photothermal materials [30,96]. In one example, an ultraviolet-laser-marked copper sheet carries a microgroove array 50–300 μm wide. Chemical oxidation then grows $Cu(OH)_2$ nanowires, which are converted into fluorinated Cu-MOF nanowhiskers. The microgrooves serve as both light-trapping cavities and mechanical "armor" for the nanostructures, and the narrow 0.88 eV bandgap of Cu-MOF enhances near-infrared absorption. The surface achieves solar absorptance above 98%, delays icing by 3960 s at −18 °C, and melts accreted ice within 720 s under one sun [95].

The fourth category is low-surface-energy functionalization. Fluorosilane vapor deposition is the most common. Self-assembled monolayers of thiols or stearic acid are

alternatives. Infusing lubricants such as silicone oil into porous structures yields slippery liquid-infused porous surfaces (SLIPSs) [97]. The interfacial slipperiness mimics the lubricant layer of pitcher plants. SLIPS are lubricant-infused rather than superhydrophobic surfaces and are not discussed further.

3.6. Comparison and Selection

Table 2 summarizes the key parameters of the above laser schemes for horizontal comparison in terms of precision, throughput, performance, and applicable scenarios.

Table 2. Typical characteristics and performance comparison of different laser fabrication schemes.

Laser Type	Femtosecond	Picosecond	Nanosecond	Continuous Wave
Pulse width	10^{-15} s	10^{-12} s	10^{-9} s	Continuous
Mechanism	Cold ablation (nonlinear)	Thermal–nonthermal hybrid	Thermally confined ablation	Photothermal–chemical conversion
Typical morphology	LIPSS; three-level hierarchy	Honeycomb micropits + reticulated papillae hierarchy	Microcone arrays	Porous graphene network
Processing speed	Low (mm/s)	Moderate (cm/s)	High (m/s)	Moderate
UV–Vis–NIR absorptance	>90% over 200–1100 nm [26]	>70% over visible–NIR [98]	AM1.5-weighted 97.97% over 300–2500 nm [75]	≈98% over 300–2500 nm [78]
Water contact angle (after modification)	≈162° (sliding angle ≈ 3°) [26]	≈157° [98]	≈160° [75]	≈165° (after silanization) [78]
Photothermal temperature rise (1 sun, test conditions)	35 → ≈83 °C after 300 s, starting near-ambient [26]	Reaches ≈ 72 °C (bare Al ≈ 40 °C); time to steady state not reported [98]	ΔT ≈ 35 °C under 1 sun; starting temperature and duration not reported [75]	Reaches ≈ 65 °C after 15 min, starting near ambient [78]
Main advantages	Highest precision; material-universal	Balance of precision and throughput	High throughput; low cost	Dual-mode heating (photo + electrothermal); flexible
Main limitations	Low throughput; high cost	Cost higher than nanosecond	Insufficient nanoscale roughness	Carbon-rich substrates only; wear resistance to be improved

Note: The "photothermal temperature rise" row of Table 2 follows the format "1 sun (100 mW/cm^2), initial ambient temperature, illumination duration, and reached temperature". The arrow "→" denotes the increase from the initial temperature to the temperature reached after the stated illumination duration. Because irradiance calibration, spectral band, illumination time, substrate, and ambient conditions differ across the cited studies, the values in this table are not directly comparable across columns and should be read as indicative ranges under the stated conditions. Quantitative cross-route comparison requires the standardized protocol in Section 5.4.

The selection among laser schemes depends on the area, cost, and performance targets (Table 2). Continuous-wave direct texturing suits very large-area components with moderate absorption requirements. Nanosecond lasers suit general large-area metal surfaces. Picosecond lasers balance higher absorption against moderate area. Femtosecond lasers apply to metallic and non-metallic substrates and meet submicron-precision needs. Continuous-wave LIG supports dual-mode heating, flexibility, and anti-icing on curved surfaces. Hybrid manufacturing is an important trend for reconciling performance and cost.

4. Anti-Icing and Deicing

Laser-based photothermal superhydrophobic surfaces form a "repel–melt–drain" closed loop through the synergy, rather than simple superposition, of passive water repellency and active photothermal deicing.

4.1. Passive Anti-Icing

Passive anti-icing constitutes the first line of defense and comprises three barriers.

The first barrier suppresses ice nucleation. The Cassie–Baxter state reduces the solid–liquid contact area and the density of heterogeneous nucleation sites. The nucleation-delay time increases as the solid–liquid contact area fraction decreases, showing that structural design can regulate anti-nucleation capability. For example, a femtosecond-laser-built dual-energy-barrier micro/nanostructure can extend the icing delay beyond 27,000 s, with an ice-adhesion strength as low as 0.9 kPa [27] (Figure 5A,B).

The second barrier is rapid droplet detachment. A low contact-angle hysteresis (<5°) and a low sliding angle (<10°) allow droplets to roll off before freezing. When the impact Weber number is below the Cassie–Wenzel transition threshold, the surface can repel impacting droplets. Raindrops reach a terminal velocity of about 9 m/s, whereas aerospace supercooled droplets impact at higher speeds, so these conditions cannot be directly compared. Superamphiphobic surfaces that combine ultrafast-laser texturing with wet-chemical deposition further extend repellency to low-surface-tension liquids, and their honeycomb composite structures also improve mechanical durability [98].

The third barrier is thermal insulation by the air layer. The air layer trapped in the surface structure has low thermal conductivity and slows heat exchange between a supercooled droplet and the cold substrate, further delaying icing. Structural design can also maintain the air pockets throughout the icing–deicing cycle. A femtosecond-laser-fabricated hierarchical structure of pitted submillimeter pillars and micropits promotes ice formation in the Cassie state, with an icing delay of 3552 s and an ice-adhesion strength as low as 1.8 kPa. The ice layer can be removed at a tilt of 10° or in a 48 m/s wind [99].

However, all these defenses presuppose an intact Cassie state. Prolonged droplet residence or condensate filling of structural cavities causes Cassie-state failure [27,100]. Frost formation is particularly damaging because vapor can nucleate inside the texture and bypass the air cushion altogether (Figure 5C). Structural reinforcement can partially mitigate the problem. Femtosecond-laser zigzag scanning can fabricate periodically bent wavy microwalls. The morphological asymmetry of the two sides deflects the liquid front's projected direction, providing extra breakthrough resistance from surface tension and raising the air-pocket breakthrough pressure to 61 kPa [101]. Texture and coating chemistry are also coupled, and a textured superhydrophobic state does not, by itself, guarantee anti-icing [102]. This is why active photothermal functionality is introduced.

4.2. Active Deicing

The passive defense described above acts before icing. Once an ice layer has formed, the photothermal effect takes over for active deicing. The surface absorbs light and converts it to heat, which is conducted to the ice–substrate interface and melts the interfacial ice into a lubricating water film. The ice–substrate contact thereby changes from solid–solid to solid–liquid–solid, the ice adhesion drops [18], and the ice layer detaches more easily.

One-dimensional energy conservation can estimate the photothermal melting time of the ice layer to the order of magnitude. Denoting the ice-layer thickness by δ, the ice density and latent heat of fusion by ρ_{ice} and L_{f}, and lumping the convective, radiative, and substrate-conduction losses into q_{loss}, the time required to melt this ice layer can be approximated as:

$$t_{\mathrm{melt}} \approx \rho_{\mathrm{ice}} L_{\mathrm{f}} \delta / (\alpha_{\mathrm{solar}} I - q_{\mathrm{loss}}) \tag{7}$$

Note that Equation (7) describes the melting of the bulk ice layer rather than the initiation of interfacial melting; the latter is governed by the much shorter thermal-diffusion time required for the interface to reach 0 °C. The model assumes one-dimensional heat flow normal to the substrate, constant thermophysical properties and net heat flux, and negligible sensible heat (warming the ice from a subcooling of 10–20 °C to 0 °C requires only about 6–13% of the latent heat). Equation (7) shows that increasing the AM1.5-weighted absorptance and reducing

heat loss are equivalent ways to shorten the melting time. Taking a 1 mm ice layer under one sun (1000 W/m^2) with the heat loss estimated at 100 W/m^2 as an example, increasing the absorptance from 0.30 to 0.95 shortens the melting time estimated by Equation (7) from about 25 min to about 6 min. Experimentally, a photothermal superhydrophobic surface combining laser-ablated microgrooves with a TiN@SiO_2 armor shows a one-sun temperature rise of 35 °C and melts the ice layer within 179 s [75]. A mosquito-eye-inspired microspike array combined with candle soot melts accumulated snow outdoors at −9.6 °C within 522 s and removes an 8 mm ice layer within 1359 s [76].

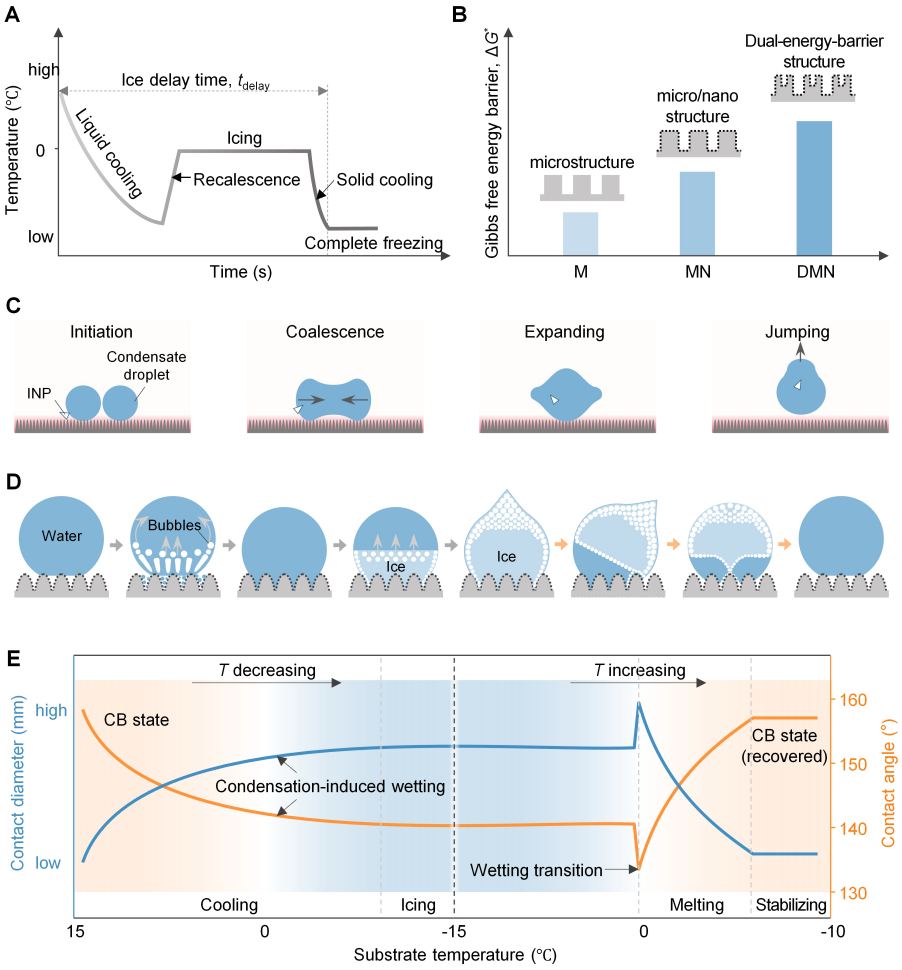

Figure 5. Structural design strategies for anti−icing and photothermal deicing. (**A**) Schematic cooling curve of a sessile droplet defining the ice delay time t_{delay}; the recalescence plateau marks ice nucleation. (**B**) Gibbs free energy barrier (ΔG) to ice nucleation on microstructured (M), micro/nanostructured (MN), and dual−energy−barrier (DMN) surfaces. (**C**) Condensation frosting on a textured surface, from initiation at ice−nucleating particles through coalescence and expansion to coalescence−induced droplet jumping. Schematic inspired by [103]. (**D**) Photothermal deicing sequence: interfacial melting with vapor/bubble generation, ice−cap detachment and sliding, and meltwater beading on the restored water−repellent surface. Redrawn and adapted from Wang et al. [100], licensed under CC BY 4.0. (**E**) Wettability evolution over a full cooling−icing−melting−stabilizing cycle, with contact diameter (blue) and contact angle (orange) tracking condensation−induced Cassie−Baxter−state degradation and its recovery after deicing. Redrawn and adapted from Wang et al. [55], licensed under CC BY 4.0.

Coupling photothermal conversion with superhydrophobicity can prevent refreezing. On a purely photothermal surface, meltwater tends to spread and refreeze after illumination stops. On a photothermal superhydrophobic surface, the meltwater beads up and rolls off, keeping the

interface dry, an advantage no single mechanism can achieve (Figure 5D,E). Physically, during melting, air bubbles inside the ice impact the micro/nanovalleys under the Marangoni force and restore the air pockets, driving a spontaneous Wenzel-to-Cassie reversal [100].

The values in Table 3 were obtained under different test conditions and should not be used for strict cross-study ranking. They indicate orders of magnitude and highlight the need for the characterization standardization discussed in Section 5.4 (CNT, carbon nanotube; CA, contact angle; SA, sliding angle).

Table 3. Summary of key performance of representative photothermal/superhydrophobic anti-icing surfaces.

Representative System/Structure	Wetting (CA/SA)	Passive Anti-Icing (Icing Delay/Ice Adhesion)	Photothermal or Hybrid Deicing	Test Conditions and Limitations
Nanosecond/UV-laser thermally confined textured metals (stainless-steel microgrooves + TiN@SiO_2; copper microspikes + candle soot)	CA ≈ 155–160° [75,76]	Not reported	1-sun ΔT ≈ 35–45 °C; ice melted within 179 s [75]; outdoors at −9.6 °C, snow melted within 522 s and an 8 mm ice layer removed within 1359 s [76]	1-sun tests use solar simulators; outdoor deicing used uncalibrated natural sunlight; values across systems are not directly comparable
Picosecond-laser copper textures (coral-like porous/papilla arrays)	CA 161°, SA 1° after aging [104]	Not reported	Peak visible absorptance 97%; average > 90% over 250–2500 nm [69]; no 1-sun temperature rise reported	Optical and wetting data come from different samples; no photothermal test
Hydrophobic LIG line arrays and superhydrophobic LIG composites	CA 134.7–147.8° [54]; after fluorination CA 161.2°, SA ≈ 1.6° [83]	Icing delay extended from 106 s to 868 s at −15 °C [83]	Joule heating to 100 °C within 15 s [54]; superhydrophobic/electrothermal composite saves 48.75% (static) and 17.4% (dynamic) energy vs. pure electric heating [83]	Joule heating is electrically driven, not 1-sun photothermal; restricted to carbon-rich substrates
Ni-decorated LIG hierarchical surface	CA 162.6° [84]	Icing delay 224.8 s [84]	Multimodal deicing in 63.2 s (light), 56.2 s (electrical), and 83.0 s (magnetic) [84]; post-abrasion electrodeposition repairs the worn surface	The three deicing modes were tested separately rather than under 1 sun; superhydrophobicity relies on fluorination
Silicone-rubber/CNT hot-embossed coating (non-laser reference)	CA 168.6°, SA 4.6° [68]	Ice adhesion ≈ 15.3 kPa [68]	Under standard solar illumination, surface rises from ≈22 °C to ≈86 °C within 5 min; deicing rate 0.92 mg/s [68]	Non-laser reference system included for comparison only

The representative systems listed in Table 3, together with the hierarchical-surface data cited in the text, demonstrate the co-directional relationship among structural parameters, full-spectrum absorption, and wetting/ice-adhesion performance, providing an evidence framework for structural homology.

4.3. Weak-Light and Light-Free Operation

The performance gains of full-spectrum, high-absorption surfaces under weak irradiance require careful qualification. Conventional coatings rely on the material's intrinsic absorption and usually cover only part of the spectrum, whereas laser-textured surfaces raise full-spectrum-weighted absorptance through geometric light trapping. Because the steady-state temperature rise is approximately linear with incident irradiance, lower irradiance yields a proportionally smaller temperature rise. Insufficient heating on overcast days is therefore a common constraint for all photothermal schemes [105].

The absorptance of a laser-textured surface is determined by its morphology and does not change with the irradiance [33,74], so its temperature-rise advantage over conventional

blackened coatings and bare metals is preserved at low irradiance. Two practical limits remain. Interfacial melting cannot start below the energy-balance irradiance threshold, and re-entrant overhangs lose their ice-adhesion advantage once contaminated or damaged.

This difference matters especially in cold, high-latitude regions, where the axial tilt keeps the winter sun low and the day short (Figure 6A). Sunlight there arrives at oblique incidence for most of the day (the solar incidence angular constraint), and overcast days are frequent, so systems that rely on strong light cannot operate for long periods. The right-hand map quantifies this constraint: in boreal winter (December–February), the mean daytime irradiance falls below about 0.3 sun across most mid-to-high-latitude land, much of which simultaneously remains sub-freezing. The steady-state temperature rise in Equation (6) therefore falls to a corresponding fraction of its one-sun value. Full-spectrum high-absorption structures can exploit diffuse skylight and low-angle sunlight to partially sustain function, typically holding the surface near the freezing point to extend the icing delay rather than achieving complete deicing. Breaking the constraint itself calls for geometry-adaptive designs: a Janus architecture pairing photon-capturing protrusions with thermally insulating recesses achieves complete deicing even at 0.1 sun, 60° incidence, and −20 °C [32].

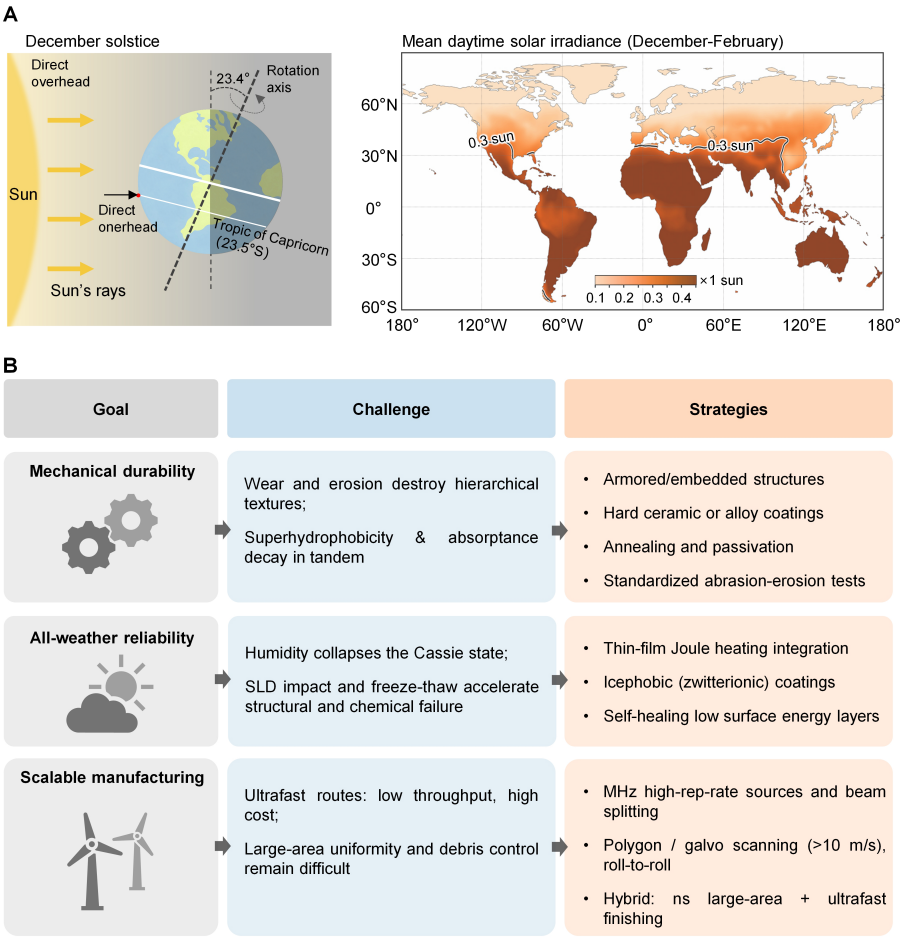

Figure 6. Solar-resource constraints and engineering outlook for laser-textured photothermal anti-/deicing surfaces. (**A**) Origin and magnitude of the winter solar-resource constraint. (**Left**): At the December solstice, the 23.4° tilt of the rotation axis places direct overhead sunlight over the Tropic of Capricorn, leaving northern mid-to-high latitudes at low solar elevation and oblique incidence. (**Right**): Mean daytime solar irradiance over land in December–February, normalized to the 1-sun reference of 1000 W/m^2, plotted by the authors using the NASA POWER and CERES SYN1deg climatology datasets (2001–2020; U.S. NASA public open data), with the contour marking 0.3 sun. (**B**) For each of the three engineering bottlenecks (mechanical durability, all-weather reliability, and scalable manufacturing), the failure origins (challenge) are paired with feasible countermeasures (strategies).

Completely light-free conditions (night, polar night, or shading by ice accretion) remain a hard boundary for purely photothermal schemes and require non-optical energy input. Candidate routes include photothermal/electrothermal dual-mode switching via LIG-type conductive networks (Section 3.4), phase-change heat storage for night-time release [106], and wind-assisted meltwater shedding, with early demonstrations in laser-textured dual-mode coatings [107,108]. Most remain at the proof-of-concept stage and require systematic energy accounting.

5. Challenges and Perspectives

Beyond these solar-resource constraints, laser-based photothermal superhydrophobic anti-icing surfaces still face three bottlenecks in mechanical durability, all-weather reliability, and scalable manufacturing. Mechanical wear simultaneously destroys the light-trapping structure and the Cassie air layer. Low-temperature, high-humidity failure limits adaptability to complex conditions, and manufacturing cost determines whether the technology can be adopted in large-area infrastructure. Figure 6B summarizes the failure origins and countermeasures for the three bottlenecks.

5.1. Mechanical Durability Bottleneck

Hierarchical micro/nanostructures are mechanically fragile; their high specific surface area and stress-concentrating sites make them vulnerable to abrasion, sand erosion, and external forces. This damage weakens light absorption and hydrophobicity simultaneously and is the first problem to solve. Protection strategies fall into three categories. The first, interfacial and matrix strengthening, is illustrated by an interfacial design inspired by gecko-foot bristles, which improves the adhesion strength of laser-direct-written coatings [109]. The second, bulk-structure strengthening, reinforces the texture itself. For instance, a laser-textured honeycomb micropit array retains a contact angle above 150° after 20 sandpaper-abrasion cycles [110]. The third, armored-frame protection, shields the nanoscale roughness under a rigid microframe. A MOF coating on a laser-etched honeycomb skeleton retains a contact angle of about 145° and an icing delay above 2400 s after 200 abrasion cycles [30]. A complementary strategy repairs rather than protects. Post-abrasion electrodeposition rebuilds the Ni-rich functional layer on the retained LIG framework and restores multimodal deicing [84]. Yet standard tests for cyclic abrasion, erosion, and thermal shock remain undefined. Even surfaces that pass laboratory abrasion tests are hard to repair in the field. Durability therefore determines service life and maintenance cost.

5.2. All-Weather Service Reliability

Constant temperature, humidity, and illumination in the laboratory poorly represent real-world conditions. All-weather reliability is constrained by three main conditions. Sustained high humidity degrades the Cassie state. Supercooled large droplet (SLD) impact tests both surface repellency and melting capacity. Repeated freeze–thaw cycles accelerate structural and chemical failure [102]. A season-adaptive radiative-cooling–photothermal superhydrophobic metasurface reconciles the conflict between summer heat dissipation and winter anti-icing, achieving a 4.6-fold longer icing delay and a 51% shorter melting time [111]. For harsh conditions such as supercooled droplet impact, a full-spectrum photothermal nanocomposite surface reaches an equilibrium temperature rise of 65.1 °C under one sun. It completes photothermal deicing within 6 min when mounted on a rotating three-blade propeller, and remains effective under simulated SLD spraying (−20 °C, droplet diameter of 62.57 μm) [112].

Countermeasures include integrating thin-film electrothermal elements on laser-textured surfaces [113], introducing icephobic coatings such as zwitterionic polymers, and developing self-healing surfaces that restore hydrophobicity after damage. A photoelectric-synergistic flexible solid slippery surface maintains low ice adhesion at −80 °C and self-heals at low temperatures, offering a material-level solution for all-weather anti-icing [114]. A recently reported transparent self-lubricating anti-icing coating combines molecular-scale jigsaw assembly with a macroscopic interpenetrating polymer network in a multiscale complementary design, achieving both low ice adhesion (about 30 kPa) and wear resistance (thickness loss of only about 80 μm after 800 Taber-abrasion cycles). It is highly transparent and causes almost no power-generation loss when coated on photovoltaic panels [115].

5.3. Industrial Scalability of Manufacturing

Industrial scale-up is the key to practical deployment. The throughput and cost limits of femtosecond lasers are evident. Throughput can be increased with MHz-repetition-rate fiber lasers, beam splitting, polygon-mirror/high-speed galvanometer scanning, and roll-to-roll processing. On the source side, industrial picosecond lasers have reached an average power of 420 W [116]. On the process side, direct laser interference patterning can fabricate high-aspect-ratio periodic structures over large areas [117], roll-to-roll laser manufacturing can continuously produce breathable superhydrophobic membranes [118], and laser-direct-written templates combined with replica molding can mass-produce high-aspect-ratio superhydrophobic microcilia arrays [119].

In high-value scenarios such as aerospace and offshore wind power, the long service life and maintenance-free advantages can offset the initial investment. Cost-sensitive scenarios such as ships and buildings are better served by a hybrid scheme of "large-area nanosecond texturing + local ultrafast-laser finishing", and film and web components can adopt roll-to-roll continuous laser manufacturing.

5.4. Characterization Standardization

Inconsistent characterization and reporting also constrain development in this field. Temperature-rise tests are run under widely different light sources, irradiances, angles, and durations, making the data hard to compare. Thermal emissivity is often missing, preventing any assessment of steady-state temperature rise and radiative heat loss (see Section 2.3). The most acute gap, however, lies in the near-infrared. Routine UV–Vis spectrophotometers typically cover only 250–1100 nm, whereas the 1100–2500 nm region carries roughly one-fifth of AM1.5 solar energy. Measuring this region requires a UV–Vis–NIR instrument with an integrating sphere, so researchers often omit it. Many published "high-absorption" claims therefore cannot be converted into AM1.5-weighted absorptance. This data gap, rather than any disagreement on physics, is the main obstacle to comparing photothermal surfaces across laboratories today.

A unified reporting framework is therefore recommended to improve data comparability and better quantify the structure–wavelength matching criterion. At minimum, each report should include three datasets. Optical characterization should cover 250–2500 nm absorption/reflection spectra, AM1.5-weighted absorptance, and thermal emissivity. Test conditions should specify the illumination (light source, irradiance, angle, and duration) and the icing environment (ice type, temperature and humidity, droplet size, and impact velocity). For ice adhesion, the report should also specify the testing method (e.g., shear versus tensile push-off), test temperature, ice–substrate contact area, and loading rate, as measured values depend strongly on all four. Durability should be documented as performance retention after abrasion, freeze–thaw, and ultraviolet aging.

5.5. Future Directions

Looking ahead, frontier research should directly support quantifying and engineering the "spectral-engineering bridge" rather than indiscriminately introducing new concepts.

First, inverse design of full-spectrum hierarchical structures for weak-light conditions should be considered. Machine learning and multiphysics simulations should jointly optimize the AM1.5-weighted absorptance, contact-angle hysteresis, ice adhesion, and aspect ratio, inverting the target operating conditions into combinations of structural sizes and periods. Biological prototypes such as moth eyes and papilionid wing scales provide validated targets for this inversion. A practical bottleneck, however, is the data itself. The reporting inconsistencies identified in Section 5.4 mean that literature data pooled across studies are noisy and weakly comparable, so the near-term value of machine learning depends as much on standardized, machine-readable datasets as on model sophistication.

Second, intelligent anti-icing systems built around the "repel–melt–drain" loop, coupling temperature/humidity, illumination, and ice-layer sensing with sunlight, Joule heating, and stored-heat release, can achieve switching at the lowest energy cost.

Third, green and sustainable manufacturing, including fluorine-free hydrophobization, laser secondary aging promotion, recyclable substrates, and low-energy continuous-wave/nanosecond processes, can be considered. For energy-intensive ultrafast-laser processing, the performance gain per unit area can be weighed against the energy cost to assess its environmental justification.

6. Conclusions

This review surveys the theory, processing, and applications of laser-fabricated biomimetic photothermal superhydrophobic anti-icing surfaces. Three conclusions can be drawn. Hierarchical micro/nanoroughness is the shared geometric platform of light absorption and superhydrophobicity, and within a moderate aspect-ratio window, greater hierarchy strengthens both light trapping and Cassie stability. Evaluation of photothermal performance used AM1.5-weighted absorptance α_{solar}, not visible-band absorptance alone, with structure–wavelength matching as the design criterion. The "repel–melt–drain" loop is physically closed. Superhydrophobicity delays nucleation and sheds droplets, photothermal heating melts interfacial ice, and the Cassie state expels meltwater before refreezing.

On the manufacturing side, the four laser routes occupy complementary positions. Femtosecond lasers excel in precision, picosecond lasers balance performance and throughput, nanosecond lasers suit large-area, high-throughput processing, and continuous-wave lasers offer industrial throughput, LIG conversion, and secondary treatment.

Several constraints remain before translation to practice: mechanical wear, which simultaneously removes the optical and wetting functions; all-weather reliability under sustained humidity, SLD impact, and freeze–thaw fatigue; manufacturing cost; and the characterization inconsistencies identified in Section 5.4. Reported ice-adhesion values for similar structures span one to two orders of magnitude, and quantitative comparison awaits the standardized, full-spectrum reporting called for there.

A critical reading of the evidence sharpens these conclusions. Among the routes reviewed, nanosecond-laser texturing combined with low-surface-energy modification currently has the most convincing experimental basis, as it has been demonstrated on the largest areas and reproduced on multiple substrates. Femtosecond processing offers the finest feature control, but the lowest throughput, and its long-term durability remains the least documented. Three problems remain unsolved across all routes. First, no study has yet shown that high AM1.5-weighted absorptance and the Cassie state survive together after standardized abrasion, erosion, or freeze–thaw testing. Second, reported ice-adhesion values for similar structures span one to two orders of magnitude and cannot be compared

rigorously until the reporting framework of Section 5.4 is adopted. Third, photothermal deicing has been validated almost exclusively under laboratory solar simulators; given the winter solar-resource constraint analyzed above, field validation, rather than recording laboratory values, is the decisive next step.

In the near term, pilot demonstrations on high-value components such as aircraft parts and offshore wind-turbine blade-leading edges are realistic; in the medium term, nanosecond/continuous-wave large-area processing can be extended to transmission towers and full-size blades; and in the long term, once fluorine-free modification, parallel processing, and standardized testing mature, the technology can spread to cost-sensitive scenarios such as ships and buildings. The structural-homology perspective and the spectral-engineering-bridge framework are expected to help the field move from demonstrating isolated recorded values to engineering predictable, comparable, and durable anti-icing surfaces.

Author Contributions: Conceptualization, C.G.; writing—original draft preparation, C.G.; writing—review and editing, C.G., Y.L. and Y.D.; supervision, C.G. and Y.L.; writing—review and editing, C.G., Y.L. and Y.D.; funding acquisition, C.G. All authors have read and agreed to the published version of the manuscript.

Funding: This work was supported by the Taizhou Municipal Science and Technology Project of the Taizhou Municipal Science and Technology Bureau (Grant No. 25gya18), the General Research Project of the Department of Education of Zhejiang Province (Grant No. Y202558549), and the High-level Talent Introduction Research Initiation Grant Program of Taizhou Vocational and Technical College (Grant No. 2025GCC04, No. 2025GCC26).

Data Availability Statement: No new data were created or analyzed in this study. Data sharing is not applicable to this article.

Conflicts of Interest: The authors declare no conflicts of interest.

Abbreviations

The following abbreviations are used in this manuscript:

AM	Air mass
CA	Contact angle
CB	Cassie–Baxter
CW	Continuous wave
DMN	Dual-energy-barrier micro/nanostructure
INP	Ice-nucleating particle
LIFT	Laser-induced forward transfer
LIG	Laser-induced graphene
LIPSS	Laser-induced periodic surface structure
LSPR	Localized surface plasmon resonance
M	Microstructured
MIR	Multiple internal reflection
MN	Micro/Nanostructured
MOF	Metal–organic framework
NIR	Near-infrared
PDMS	Polydimethylsiloxane
SA	Sliding angle
SLD	Supercooled large droplet
SLIPS	Slippery liquid-infused porous surface
SPP	Surface plasmon polariton

References

1. Yamazaki, M.; Jemcov, A.; Sakaue, H. A Review on the Current Status of Icing Physics and Mitigation in Aviation. *Aerospace* **2021**, *8*, 188. [CrossRef]
2. Parent, O.; Ilinca, A. Anti-icing and de-icing techniques for wind turbines: Critical review. *Cold Reg. Sci. Technol.* **2011**, *65*, 88–96. [CrossRef]
3. Ensikat, H.J.; Ditsche-Kuru, P.; Neinhuis, C.; Barthlott, W. Superhydrophobicity in perfection: The outstanding properties of the lotus leaf. *Beilstein J. Nanotechnol.* **2011**, *2*, 152–161. [CrossRef]
4. Clapham, P.B.; Hutley, M.C. Reduction of Lens Reflexion by the "Moth Eye" Principle. *Nature* **1973**, *244*, 281–282. [CrossRef]
5. Yang, X.; Ran, H.; Jiang, Y.; Lu, Z.; Wei, G.; Li, J. Fine structure of the compound eyes of the crepuscular moth Grapholita molesta (Busck 1916) (Lepidoptera: Tortricidae). *Front. Physiol.* **2024**, *15*, 1343702. [CrossRef]
6. McCoy, D.E.; Feo, T.; Harvey, T.A.; Prum, R.O. Structural absorption by barbule microstructures of super black bird of paradise feathers. *Nat. Commun.* **2018**, *9*, 1. [CrossRef]
7. Davis, A.L.; Nijhout, H.F.; Johnsen, S. Diverse nanostructures underlie thin ultra-black scales in butterflies. *Nat. Commun.* **2020**, *11*, 1294. [CrossRef]
8. Stratakis, E.; Bonse, J.; Heitz, J.; Siegel, J.; Tsibidis, G.; Skoulas, E.; Papadopoulos, A.; Mimidis, A.; Joel, A.C.; Comanns, P.; et al. Laser engineering of biomimetic surfaces. *Mater. Sci. Eng. R* **2020**, *141*, 100562. [CrossRef]
9. Lian, Z.; Zhou, J.; Ren, W.; Chen, F.; Xu, J.; Tian, Y.; Yu, H. Recent progress in bio-inspired macrostructure array materials with special wettability—From surface engineering to functional applications. *Int. J. Extrem. Manuf.* **2024**, *6*, 012008. [CrossRef]
10. Yue, L.; Chen, G.; Zhou, J.; Li, S.; Song, R.; Zheng, X.; Wang, B.; He, Q.; Xie, S. Review of Anti-/De-Icing Strategies Based on Ice Nucleation and Growth Mechanism and Their Applications. *Adv. Funct. Mater.* **2026**, *36*, e76934. [CrossRef]
11. Zhao, L.; Shen, Y.; Tao, J.; Liu, W.; Wang, T.; Liu, S. Review on Icephobicity of Materials Surface Enhanced by Interface Action Force. *Adv. Mater. Interfaces* **2024**, *12*, 2400665. [CrossRef]
12. Chen, Z.; Yang, J.; Liu, H.; Zhao, Y.; Pan, R. A short review on functionalized metallic surfaces by ultrafast laser micromachining. *Int. J. Adv. Manuf. Technol.* **2022**, *119*, 6919–6948. [CrossRef]
13. Volpe, A.; Gaudiuso, C.; Ancona, A. Laser Fabrication of Anti-Icing Surfaces: A Review. *Materials* **2020**, *13*, 5692. [CrossRef]
14. Li, K.; Zhang, Y.; Wang, X.; Li, W.; Xu, Z.; He, Q. Advances in the application of laser-fabricated superhydrophobic surfaces in efficient anti/de-icing strategies. *Prog. Org. Coat.* **2026**, *221*, 110537. [CrossRef]
15. Yao, B.; Zhang, F.; Song, M.; Chen, M. Superhydrophobic Solar Thermal Anti-Icing/Deicing: Opportunities and Challenges. *Small* **2026**, *22*, e73254. [CrossRef]
16. Shi, J.; Ke, S.; Wang, F.; Wang, W.; Wang, C. Recent advances in photothermal anti-/de-icing materials. *Chem. Eng. J.* **2024**, *481*, 148265. [CrossRef]
17. Xue, Y.; Verdross, P.; Liang, W.; Woodward, R.T.; Bismarck, A. Breaking the ice: Applications of photothermal superhydrophobic materials for efficient deicing strategies. *Adv. Colloid Interface Sci.* **2025**, *341*, 103489. [CrossRef]
18. Gao, C.; Liu, Y.; Du, Y. Water-Lubricated Photothermal Surfaces for Anti-Icing and Deicing. *Lubricants* **2026**, *14*, 201. [CrossRef]
19. Her, T.-H.; Finlay, R.J.; Wu, C.; Deliwala, S.; Mazur, E. Microstructuring of silicon with femtosecond laser pulses. *Appl. Phys. Lett.* **1998**, *73*, 1673–1675. [CrossRef]
20. Baldacchini, T.; Carey, J.E.; Zhou, M.; Mazur, E. Superhydrophobic surfaces prepared by microstructuring of silicon using a femtosecond laser. *Langmuir* **2006**, *22*, 4917–4919. [CrossRef]
21. Yoon, T.O.; Shin, H.J.; Jeoung, S.C.; Park, Y.I. Formation of superhydrophobic poly(dimethylsiloxane) by ultrafast laser-induced surface modification. *Opt. Express* **2008**, *16*, 12715–12725. [CrossRef]
22. Li, B.J.; Zhou, M.; Yuan, R.; Cai, L. Fabrication of titanium-based microstructured surfaces and study on their superhydrophobic stability. *J. Mater. Res.* **2008**, *23*, 2491–2499. [CrossRef]
23. Kietzig, A.M.; Hatzikiriakos, S.G.; Englezos, P. Patterned Superhydrophobic Metallic Surfaces. *Langmuir* **2009**, *25*, 4821–4827. [CrossRef]
24. Lin, J.; Peng, Z.; Liu, Y.; Ruiz-Zepeda, F.; Ye, R.; Samuel, E.L.G.; Yacaman, M.J.; Yakobson, B.I.; Tour, J.M. Laser-induced porous graphene films from commercial polymers. *Nat. Commun.* **2014**, *5*, 5714. [CrossRef]
25. Long, J.; Wu, Y.; Gong, D.; Fan, P.; Jiang, D.; Zhang, H.; Zhong, M. Femtosecond laser fabricated superhydrophobic copper surfaces and their anti-icing properties. *Chin. J. Lasers* **2015**, *42*, 0706002. [CrossRef]
26. Zhao, W.; Xiao, L.; He, X.; Cui, Z.; Fang, J.; Zhang, C.; Li, X.; Li, G.; Zhong, L.; Zhang, Y. Moth-eye-inspired texturing surfaces enabled self-cleaning aluminum to achieve photothermal anti-icing. *Opt. Laser Technol.* **2021**, *141*, 107115. [CrossRef]
27. Wang, L.; Li, D.; Jiang, G.; Hu, X.; Peng, R.; Song, Z.; Zhang, H.; Fan, P.; Zhong, M. Dual-Energy-Barrier Stable Superhydrophobic Structures for Long Icing Delay. *ACS Nano* **2024**, *18*, 12489–12502. [CrossRef]
28. Zhou, M.; Zhang, L.; Zhong, L.; Chen, M.; Zhu, L.; Zhang, T.; Han, X.; Hou, Y.; Zheng, Y. Robust Photothermal Icephobic Surface with Mechanical Durability of Multi-Bioinspired Structures. *Adv. Mater.* **2024**, *36*, 2305322. [CrossRef]

29. Song, X.; Yin, K.; Li, X.; Wang, L.; Yang, P.; Pei, J.; Huang, Y.; Arnusch, C.J.; Li, G. Efficient anti-icing/deicing via photothermal-wind synergistic effects on femtosecond laser-induced superhydrophobic graphene. *J. Mater. Chem. A* **2025**, *13*, 205–213. [CrossRef]
30. Zhou, Y.; Pei, K.; Zhou, Z.; Zhang, L.; Tan, C.; Han, X.; Yang, G.; Wu, B.; Fu, J.; Guo, Z.; et al. Synergistic solar-thermal icephobic armor: Ultrasmall-bandgap MOFs drive efficient anti-/de-icing via superhydrophobic photothermal cooperation. *eScience* **2026**, *6*, 100539. [CrossRef]
31. Zhang, C.; Liu, B.; Chen, Y.; Sun, L.; Yan, M.; Liu, Q.; Song, C.; Zhang, S.; Song, J.; Liu, C.; et al. Janus structure breaks the solar incidence angular constraint in photothermal anti-icing. *Nat. Commun.* **2026**, *17*, 5422. [CrossRef]
32. *ASTM G173-03(2020)*; Standard Tables for Reference Solar Spectral Irradiances: Direct Normal and Hemispherical on 37° Tilted Surface. ASTM International: West Conshohocken, PA, USA, 2020.
33. Li, H.; Shen, C.; Qiu, X.; Zhou, S.; Liu, M.; Li, C.; Zhang, H.; Zhang, Z. Template-Made Ultrahigh, Broadband, and Omnidirectional Light Absorption Surface for Enhanced Solar Energy Harvesting and Utilization. *Adv. Funct. Mater.* **2024**, *34*, 2407135. [CrossRef]
34. Li, H.; Zhou, S.; Liu, M.; Li, H.; Zhang, Z.; Li, C.; Zhang, H.; Zhang, Z. Ultrablack, Harsh-Condition-Resistant Micro-Pyramid Graphite Array for Solar Energy Harvesting and Conversion. *Small* **2026**, *22*, e73665. [CrossRef]
35. Hakamada, Y.; Cojocari, M.; Matoba, M.; Kawano, S.; Sakurai, H.; Konishi, K.; Pashnev, D.; Revanth Ayyagari, S.; Janonis, V.; Urbanowicz, A.; et al. Carbon-Coated Moth-Eye Structure: An Ultrabroadband THz-DUV Near-Perfect Absorber. *Adv. Opt. Mater.* **2025**, *13*, 2500948. [CrossRef]
36. Young, T. An essay on the cohesion of fluids. *Philos. Trans. R. Soc. Lond.* **1805**, *95*, 65–87. [CrossRef]
37. Wenzel, R.N. Resistance of solid surfaces to wetting by water. *Ind. Eng. Chem.* **1936**, *28*, 988–994. [CrossRef]
38. Cassie, A.B.D.; Baxter, S. Wettability of porous surfaces. *Trans. Faraday Soc.* **1944**, *40*, 546–551. [CrossRef]
39. Li, D.; Wang, L.; Peng, R.; Song, Z.; Liu, Z.; Chang, Z.; Zhang, H.; Fan, P.; Zhong, M. Re-Entrant Super-Repellent Metallic Structures for Robust Anti-Icing. *Adv. Sci.* **2025**, *12*, e08272. [CrossRef]
40. Wang, X.; Yang, Y.; Xuan, S.; Li, G.; Liu, J.; Song, Y.; Wang, Y.; Ge, Y.; Li, X.; Long, Y.; et al. Flexible Mushroom-Like Cross-Scale Surface with Extreme Pressure Resistance for Telecommunication Lines Anti-Icing/Deicing. *ACS Appl. Mater. Interfaces* **2025**, *17*, 5550–5561. [CrossRef]
41. Bizi-bandoki, P.; Valette, S.; Audouard, E.; Benayoun, S. Time dependency of the hydrophilicity and hydrophobicity of metallic alloys subjected to femtosecond laser irradiations. *Appl. Surf. Sci.* **2013**, *273*, 399–407. [CrossRef]
42. Ta, V.D.; Dunn, A.; Wasley, T.J.; Li, J.; Kay, R.W.; Stringer, J.; Smith, P.J.; Esenturk, E.; Connaughton, C.; Shephard, J.D. Laser textured superhydrophobic surfaces and their applications for homogeneous spot deposition. *Appl. Surf. Sci.* **2016**, *365*, 153–159. [CrossRef]
43. Yan, X.; Huang, Z.; Sett, S.; Oh, J.; Cha, H.; Li, L.; Feng, L.; Wu, Y.; Zhao, C.; Orejon, D.; et al. Atmosphere-Mediated Superhydrophobicity of Rationally Designed Micro/Nanostructured Surfaces. *ACS Nano* **2019**, *13*, 4160–4173. [CrossRef]
44. Hohlfeld, J.; Wellershoff, S.-S.; Güdde, J.; Conrad, U.; Jähnke, V.; Matthias, E. Electron and lattice dynamics following optical excitation of metals. *Chem. Phys.* **2000**, *251*, 237–258. [CrossRef]
45. Wang, L.; Jiang, G.; Tian, Z.; Chen, C.; Hu, X.; Peng, R.; Zhang, H.; Fan, P.; Zhong, M. Superhydrophobic microstructures for better anti-icing performances: Open-cell or closed-cell? *Mater. Horiz.* **2023**, *10*, 209–220. [CrossRef]
46. Jia, Y.; Li, A.; Wang, J.; Wang, X.; Zhang, F.; Guo, Q.; He, Q. Durable Ceramicization-Induced Uncoated Superhydrophobic Surfaces for Anti-Icing Propeller Edges. *Adv. Mater.* **2025**, *37*, e07777. [CrossRef]
47. Sundaram, S.K.; Mazur, E. Inducing and probing non-thermal transitions in semiconductors using femtosecond laser pulses. *Nat. Mater.* **2002**, *1*, 217–224. [CrossRef]
48. Rethfeld, B.; Sokolowski-Tinten, K.; von der Linde, D.; Anisimov, S.I. Timescales in the response of materials to femtosecond laser excitation. *Appl. Phys. A* **2004**, *79*, 767–769. [CrossRef]
49. Stoian, R.; Rosenfeld, A.; Ashkenasi, D.; Hertel, I.V.; Bulgakova, N.M.; Campbell, E.E.B. Surface charging and impulsive ion ejection during ultrashort pulsed laser ablation. *Phys. Rev. Lett.* **2002**, *88*, 097603. [CrossRef]
50. Chichkov, B.N.; Momma, C.; Nolte, S.; von Alvensleben, F.; Tünnermann, A. Femtosecond, picosecond and nanosecond laser ablation of solids. *Appl. Phys. A* **1996**, *63*, 109–115. [CrossRef]
51. Chakraborty, A.; Khetri, M.; Surampudi, A.; Gupta, M.C. Superhydrophilic and Superhydrophobic Surfaces with Reversible Wettability Using Laser Processing. *ACS Omega* **2026**, *11*, 27970–27984. [CrossRef]
52. Yi, L.; Wang, Z.; Wang, D.; Sun, S.; Tang, S.; Chang, X. Picosecond laser-induced construction of stable superhydrophobic surfaces with outstanding anti-icing characteristics on the FH40 low-temperature steel. *Appl. Surf. Sci.* **2026**, *741*, 167144. [CrossRef]
53. Fu, Y.; Soldera, M.; Wang, W.; Voisiat, B.; Lasagni, A.F. Picosecond Laser Interference Patterning of Periodical Micro-Architectures on Metallic Molds for Hot Embossing. *Materials* **2019**, *12*, 3409. [CrossRef]
54. Zhong, M.; Li, S.; Zou, Y.; Fan, H.; Jiang, Y.; Qiu, C.; Luo, J.; Yang, L. Hydrophobic Surface Array Structure Based on Laser-Induced Graphene for Deicing and Anti-Icing Applications. *Micromachines* **2024**, *15*, 285. [CrossRef]
55. Wang, L.; Zhao, H.; Zhu, D.; Yuan, L.; Zhang, H.; Fan, P.; Zhong, M. A Review on Ultrafast Laser Enabled Excellent Superhydrophobic Anti-Icing Performances. *Appl. Sci.* **2023**, *13*, 5478. [CrossRef]

56. Jee, Y.; Becker, M.F.; Walser, R.M. Laser-induced damage on single-crystal metal surfaces. *J. Opt. Soc. Am. B* **1988**, *5*, 648–659. [CrossRef]
57. Mannion, P.T.; Magee, J.; Coyne, E.; O'Connor, G.M.; Glynn, T.J. The effect of damage accumulation behaviour on ablation thresholds and damage morphology in ultrafast laser micro-machining of common metals in air. *Appl. Surf. Sci.* **2004**, *233*, 275–287. [CrossRef]
58. Mu, W.; Hou, Y.; Wu, Y.; Liu, M. Femtosecond Laser Fabrication of Biomimetic Super-Slippery Surfaces: A Review. *Adv. Eng. Mater.* **2026**, *28*, e202501596. [CrossRef]
59. Vorobyev, A.Y.; Topkov, A.N.; Gurin, O.V.; Svich, V.A.; Guo, C. Enhanced absorption of metals over ultrabroad electromagnetic spectrum. *Appl. Phys. Lett.* **2009**, *95*, 121106. [CrossRef]
60. Tao, H.-Y.; Chen, R.; Song, X.-W.; Chen, Y.-N.; Lin, J.-Q. Femtosecond laser pulse energy accumulation optimization effect on surface morphology of black silicon. *Acta Phys. Sin.* **2017**, *66*, 067902. [CrossRef]
61. Chaudhary, N.; Naraharisetty, S.R.G. Femtosecond laser-induced nanoscale texturing for super-black stainless-steel surfaces. *J. Phys. Photonics* **2026**, *8*, 025030. [CrossRef]
62. Liu, Z.; Hu, Z.; Qi, J.; Li, C.; Wang, Y.; Qian, M.; Liu, X. Fabrication of black metal surface for high solar energy absorption by femtosecond laser hybrid technology. *Opt. Express* **2024**, *32*, 38655. [CrossRef]
63. Park, M.; Verma, S.; LaPotin, A.; Nizamian, D.P.; Prasher, R.; Henry, A.; Lubner, S.D.; Grigoropoulos, C.P.; Zorba, V. High-emissivity, thermally robust emitters for high power density thermophotovoltaics. *Joule* **2025**, *9*, 102005. [CrossRef]
64. Jia, Y.; Li, A.; Xu, Z.; Qi, K.; Zhong, J.; Zhang, F.; Guo, Q.; He, Q. Laser-induced ash-deposited silicone rubber surfaces with synergistic micro/nanostructures for enhanced superhydrophobicity and anti-/de-icing performance. *Chem. Eng. J.* **2025**, *523*, 168252. [CrossRef]
65. Wen, Z.; Shi, H.; Yue, S.; Li, M.; Zhang, Z.; Wang, R.; Song, Q.; Xu, Z.; Zhang, Z.; Hou, Y. Large-Scale Black Silicon Induced by Femtosecond Laser Assisted With Laser Cleaning. *Front. Phys.* **2022**, *10*, 862605. [CrossRef]
66. Zhan, Z.; Garcell, E.M.; Guo, C. Robust mold fabricated by femtosecond laser pulses for continuous thermal imprinting of superhydrophobic surfaces. *Mater. Res. Express* **2019**, *6*, 075011. [CrossRef]
67. Sakurai, T.; Somekawa, T.; Hirai, Y.; Matsushita, H. Superhydrophobic PDMS using Femtosecond Laser-Processed Surface Molds for Anti-Icing. *J. Photopolym. Sci. Technol.* **2025**, *38*, 91–98. [CrossRef]
68. Jiang, G.; He, B.; Yang, C. Superhydrophobic anti-icing/de-icing SR/CNTs surfaces hot-embossed with femtosecond laser machined mold. *Surf. Eng.* **2024**, *40*, 895–906. [CrossRef]
69. Fan, P.; Zhong, M.; Li, L.; Huang, T.; Zhang, H. Rapid fabrication of surface micro/nano structures with enhanced broadband absorption on Cu by picosecond laser. *Opt. Express* **2013**, *21*, 11628. [CrossRef]
70. Vercillo, V.; Tonnicchia, S.; Romano, J.-M.; García-Girón, A.; Aguilar-Morales, A.I.; Alamri, S.; Dimov, S.S.; Kunze, T.; Lasagni, A.F.; Bonaccurso, E. Design Rules for Laser-Treated Icephobic Metallic Surfaces for Aeronautic Applications. *Adv. Funct. Mater.* **2020**, *30*, 1910268. [CrossRef]
71. Zhang, Z.; Hua, Y.; Ye, Y.; Chen, R.; Li, Z.; Yang, J.; Shuai, W. Fabrication of superhydrophobic nickel-aluminum bronze alloy surfaces based on picosecond laser pulses. *Chin. J. Lasers* **2019**, *46*, 0302013. [CrossRef]
72. Sun, X.; Sun, S.; Wang, H.; Wang, J.; Liu, S.; Wang, P. Preparation and process optimization of superhydrophobic surface on 7075 Al alloy based on picosecond laser. *Acta Mater. Compos. Sin.* **2023**, *40*, 3583–3593. (In Chinese) [CrossRef]
73. Lou, D.; Chen, C.; Wan, H.; Dong, C.; Wu, C.; Liu, K.; Cheng, J.; Tao, Q.; Cai, X.; Li, Q.; et al. Laser Texture Deposition of Superhydrophobic Surfaces: Fabrication and Mechanism. *Phys. Status Solidi A* **2025**, *222*, e202500593. [CrossRef]
74. Yang, J.; Luo, F.; Kao, T.S.; Li, X.; Ho, G.W.; Teng, J.; Luo, X.; Hong, M. Design and fabrication of broadband ultralow reflectivity black Si surfaces by laser micro/nanoprocessing. *Light Sci. Appl.* **2014**, *3*, e185. [CrossRef]
75. Zhang, L.; Feng, Y.; Cao, X.; Dong, Y.; Liu, W.; Li, B.; Li, J.; Hao, C. Hierarchical Icephobic Surfaces with Enhanced Photothermal Performance for Sustainable Anti-Icing. *Adv. Sci.* **2025**, *12*, 2502945. [CrossRef]
76. Zhou, M.; Zhang, T.; Wei, H.; Zhu, L.; Gao, C.; Luo, Q.; Hou, Y.; Zheng, Y. Mosquito-Eye-Inspired Photothermal Icephobic Surface with Enhanced Anti-Icing and Deicing Efficiency. *ACS Appl. Mater. Interfaces* **2025**, *17*, 37300–37310. [CrossRef]
77. An, H.; Qian, Y.; Xu, X.; Guo, H.; Wang, B.; Zhang, Z.; Jiang, M.; Huang, H.; Yan, J. Manipulating Wetting State of CFRP via One-Step Laser Micro/Nanostructuring. *Small* **2025**, *21*, e06695. [CrossRef]
78. Wang, L.; Li, J.; Chen, Z.; Song, Z.; Meng, X.; Chen, X. Porous Graphene-Based Photothermal Superhydrophobic Surface for Robust Anti-Icing and Efficient De-Icing. *Adv. Mater. Interfaces* **2022**, *9*, 2201758. [CrossRef]
79. Wang, L.; Yin, K.; Li, X.; Liu, X.; Xiao, J.; Pei, J.; Song, X. In situ construction of multifunctional femtosecond laser-induced graphene on arbitrary substrates. *Mater. Horiz.* **2025**, *12*, 5780–5790. [CrossRef]
80. Ji, H.; Yang, C.; Su, H.; Qi, Z.; Wang, Y.; Cheng, E.; Hu, N. Multifunctional superhydrophobic film with comprehensive icing monitoring, anti-icing, and photothermal/electrothermal deicing properties. *Prog. Org. Coat.* **2025**, *206*, 109337. [CrossRef]
81. Wang, L.; Yin, K.; Xiao, J.; Song, X.; Pei, J.; He, J.; Duan, J.A. Femtosecond laser synthesis of multiscale high-entropy alloys/graphene composites for high-performance Joule heating. *Nat. Commun.* **2026**, *17*, 2121. [CrossRef]

82. Liu, F.; Gao, Y.; Wang, G.; Wang, D.; Wang, Y.; He, M.; Ding, X.; Duan, H.; Luo, S. Laser-Induced Graphene Enabled Additive Manufacturing of Multifunctional 3D Architectures with Freeform Structures. *Adv. Sci.* **2023**, *10*, 2204990. [CrossRef]
83. Niu, Y.; Sun, Y.; Tao, X.; Liao, C.; Yao, J. Superhydrophobic-electrothermal laser-induced graphene for effectively anti-icing and de-icing. *Compos. Commun.* **2024**, *46*, 101830. [CrossRef]
84. Xu, H.; Luo, P.; Wang, J.-X.; Feng, J.; Tan, Z.; Lu, H.; Zhou, T. Multimodal anti-/deicing on laser-structured polymer surface via photothermal retention and post-abrasion redeposition. *Adv. Funct. Mater.* **2026**, *36*, e78297. [CrossRef]
85. Wang, L.; Yin, K.; Li, X.; Huang, Y.; Xiao, J.; Pei, J.; Song, X.; Duan, J.; Arnusch, C.J. Femtosecond Laser Ultrafast Atomic Scale Renovating Laser-Induced Graphene. *Adv. Funct. Mater.* **2025**, *35*, 2506215. [CrossRef]
86. Gao, C.; Zhang, L.; Hou, Y.; Zheng, Y. A UV-Resistant Heterogeneous Wettability-Patterned Surface. *Adv. Mater.* **2023**, *35*, 2304080. [CrossRef]
87. Zhang, K.; Huang, J.; Lu, S.; Hu, Y.; Pan, W.; Liu, L. Multi-Scale Biomimetic Strategy: Robust Woven Wires with Photo-Thermal De-Icing and Spontaneous De-Wetting. *Adv. Funct. Mater.* **2025**, *35*, 2423043. [CrossRef]
88. Chen, C.; Peng, X.; Wang, Z.; Li, J.; Jiang, R. Bioinspired Photothermal Superhydrophobic Surfaces Fabricated by Femtosecond Laser-MXene Synergy for Anti-Icing/Deicing. *Ind. Eng. Chem. Res.* **2025**, *64*, 17049–17059. [CrossRef]
89. Xu, H.; Luo, P.; Wang, J.-X.; Lu, H.; Feng, J.; Li, S.; Zhou, T. Patternable, Multifunctional Superwettable Surface with Micro/Nanostructures by Polydimethylsiloxane Polymer-Assisted Laser Direct Writing. *Adv. Funct. Mater.* **2026**, *36*, e27707. [CrossRef]
90. Yan, P.; Hou, Y.; Zheng, H.; Liu, M. Ultrafast laser-assisted hybrid fabrication of biomimetic superhydrophobic surfaces: Strategies, mechanisms, and applications. *Nanoscale* **2025**, *17*, 21400–21422. [CrossRef]
91. Gao, W.; Singh, N.; Song, L.; Liu, Z.; Reddy, A.L.M.; Ci, L.; Vajtai, R.; Zhang, Q.; Wei, B.; Ajayan, P.M. Direct laser writing of micro-supercapacitors on hydrated graphite oxide films. *Nat. Nanotechnol.* **2011**, *6*, 496–500. [CrossRef]
92. El-Kady, M.F.; Strong, V.; Dubin, S.; Kaner, R.B. Laser Scribing of High-Performance and Flexible Graphene-Based Electrochemical Capacitors. *Science* **2012**, *335*, 1326–1330. [CrossRef]
93. Bohandy, J.; Kim, B.F.; Adrian, F.J. Metal deposition from a supported metal film using an excimer laser. *J. Appl. Phys.* **1986**, *60*, 1538–1539. [CrossRef]
94. Delaporte, P.; Alloncle, A.P. Laser-induced forward transfer: A high resolution additive manufacturing technology. *Opt. Laser Technol.* **2016**, *78*, 33–41. [CrossRef]
95. Zhang, L.; Luo, B.; Fu, K.; Gao, C.; Han, X.; Zhou, M.; Zhang, T.; Zhong, L.; Hou, Y.; Zheng, Y. Highly Efficient Photothermal Icephobic/de-Icing MOF-Based Micro and Nanostructured Surface. *Adv. Sci.* **2023**, *10*, 2304187. [CrossRef]
96. Peng, X.; Tian, D.; Li, J.; Li, W.; Jiang, R.; Chen, C. Construction of Robust Electrothermal Superhydrophobic Surface via Femtosecond Laser for Anti-Icing and Deicing. *Molecules* **2025**, *30*, 1741. [CrossRef]
97. Wong, T.S.; Kang, S.H.; Tang, S.K.Y.; Smythe, E.J.; Hatton, B.D.; Grinthal, A.; Aizenberg, J. Bioinspired self-repairing slippery surfaces with pressure-stable omniphobicity. *Nature* **2011**, *477*, 443–447. [CrossRef]
98. Hou, Y.; Yan, P.; Tian, C.; Zhang, Z.; Jiang, Q.; Li, G.; Liu, M.; Guo, Z. Bioinspired photothermal superamphiphobic surface with high mechanical robustness for efficient anti/de-icing. *Chem. Eng. J.* **2026**, *532*, 174418. [CrossRef]
99. Zeng, Q.; Wang, Y.; Yang, Y.; Li, G.; Cui, Z.; Song, Y.; Liu, S.; Wang, X.; Zhou, Y.; Yin, K. Hierarchically Homo-Heterogeneous Structured Surface Promoting Effective Cassie Ice Formation for Highly Efficient Anti-/Deicing. *Adv. Funct. Mater.* **2026**, *36*, e28989. [CrossRef]
100. Wang, L.; Tian, Z.; Jiang, G.; Luo, X.; Chen, C.; Hu, X.; Zhang, H.; Zhong, M. Spontaneous dewetting transitions of droplets during icing & melting cycle. *Nat. Commun.* **2022**, *13*, 378. [CrossRef]
101. Li, L.; Zhang, B.; Xu, J.; Zou, T.; Yan, D.; Jia, Y.; He, Q.; Yang, X.; Xu, C.; Zhang, H.; et al. Resilient Cassie–Baxter state on rigid superhydrophobic surfaces by vectorizing projection of the liquid front. *J. Mater. Sci. Technol.* **2026**, *282*, 151–159. [CrossRef]
102. Gregorčič, B.; Hadžić, A.; Berce, J.; Zupančič, M.; Može, M.; Golobič, I. Bioinspired Laser-Textured Aluminum Surfaces for Anti-Icing: Coupled Effects of Hydrophobic Coating Chemistry and Surface Morphology. *Biomimetics* **2026**, *11*, 585. [CrossRef]
103. Zhang, H.; Zhao, G.; Wu, S.; Alsaid, Y.; Zhao, W.; Yan, X.; Liu, L.; Zou, G.; Lv, J.; He, X.; et al. Solar Anti-Icing Surface with Enhanced Condensate Self-Removing at Extreme Environmental Conditions. *Proc. Natl. Acad. Sci. USA* **2021**, *118*, e2100978118. [CrossRef]
104. Wang, D.; Zhang, Z.; Zhang, C.; Gu, Q.; Meng, F. Effects of picosecond laser parameters on surface wettability of cross-scale bionic mastoid-like texture. *China Surf. Eng.* **2021**, *34*, 110–119. (In Chinese) [CrossRef]
105. Yang, S.; Liu, J.; Hoque, M.J.; Huang, A.; Chen, Y.; Yang, W.; Feng, J.; Miljkovic, N. A Critical Perspective on Photothermal De-Icing. *Adv. Mater.* **2025**, *37*, 2415237. [CrossRef]
106. Chu, F.; Hu, Z.; Feng, Y.; Lai, N.; Wu, X.; Wang, R. Advanced Anti-Icing Strategies and Technologies by Macrostructured Photothermal Storage Superhydrophobic Surfaces. *Adv. Mater.* **2024**, *36*, 2402897. [CrossRef]
107. Guo, Y.; Zhao, H.; Liu, H.; Zhao, G. Laser ablated grid microstructure and carbon nanotubes (CNTs) induced superhydrophobic CNTs/epoxy composites for synergistic photothermal and electrothermal anti-icing/deicing. *Prog. Org. Coat.* **2026**, *218*, 110289. [CrossRef]

108. Liu, Q.; Wang, Y.; Liu, X.; Li, Y.; Yu, E.; Sun, Z.; Wang, L.; Zhuang, G.; Yu, J.; Liu, S. Robust and Ultra-Efficient Anti-/De-Icing Surface Engineered Through Photo-/Electrothermal Micro-Nanostructures With Switchable Solid-Liquid States. *Adv. Mater.* **2025**, *37*, 2410941. [CrossRef]
109. Cai, Z.; Miao, C.; Zhang, C.; Luo, H.; Wu, J.; Zhao, T.; Yang, H.; Fan, L.; Yang, G.; Ouyang, X.; et al. Bio-Inspired Hybrid Laser Direct Writing of Interfacial Adhesion for Universal Functional Coatings. *Adv. Funct. Mater.* **2024**, *34*, 2408354. [CrossRef]
110. Zhang, L.; Luo, Y.; Xu, J.; Liu, J. Bio-inspired photothermal superhydrophobic surface with good anti-/de-icing property and durability based on laser texturing. *Surf. Coat. Technol.* **2025**, *512*, 132398. [CrossRef]
111. Wang, T.; Pang, J.; Ren, Q.; Wu, Y.; Ding, Z.; Zhang, J.; Zhang, Y.; Gu, M. Synergistic Photothermal and Superhydrophobic Metasurface for Passive Radiative Cooling and Anti-/Deicing. *Adv. Funct. Mater.* **2026**, *36*, e77762. [CrossRef]
112. Hu, W.; Sheng, H.; Zhao, W.; Li, X.; Xu, S.; Huang, X.; Liu, H. Spectrally Engineered Hierarchical Nanocomposite Enabling Full-Spectrum Solar-Thermal Conversion and Dynamic Anti-/De-icing in Harsh Environments. *Small* **2026**, *22*, e10191. [CrossRef]
113. Wang, Y.; Liao, Z.; Zeng, Q.; Li, G.; He, Y.; Yang, Y.; Song, Y.; Wang, L.; Liu, S.; Xuan, S.; et al. Robust and Energy-Effective Electrothermal Superhydrophobic Film with Micro-Hexagonal Groove Array Structure for Anti/Deicing. *Adv. Funct. Mater.* **2026**, *36*, e14771. [CrossRef]
114. Chai, Z.; Teng, Z.; Guo, P.; He, Y.; Zhao, D.; Zuo, X.; Liu, K.; Jiang, L.; Heng, L. A Photoelectric Synergistic Flexible Solid Slippery Surface for All-Day Anti-Icing/Frosting. *Small Methods* **2025**, *9*, 2400859. [CrossRef]
115. Chen, J.; Wang, Z.; Liu, X.; Zhu, Y.; Sun, S.; Zhang, L.; Chen, D.; Chen, H. Robust and transparent self-lubricating surface for anti-icing/de-icing via a multiscale puzzle complementary strategy. *Compos. Sci. Technol.* **2026**, *285*, 111818. [CrossRef]
116. Faas, S.; Bielke, U.; Weber, R.; Graf, T. Scaling the productivity of laser structuring processes using picosecond laser pulses at average powers of up to 420 W to produce superhydrophobic surfaces on stainless steel AISI 316L. *Sci. Rep.* **2019**, *9*, 1933. [CrossRef]
117. Ränke, F.; Sallese, M.; Soldera, M.; Tabares, I.; Soldera, F.; Lasagni, A.F. Optimized Strategy for Fabricating High-Aspect-Ratio Periodic Structures Over Large Areas Using ps-Direct Laser Interference Patterning. *Adv. Eng. Mater.* **2025**, *27*, 2500570. [CrossRef]
118. Liu, H.; Zhong, H.; Yuan, Q.; Yang, R.; Kim, M.; Chan, Y.H.T.; Chen, S.; Lin, J.; Li, M.G. Roll-to-Roll Manufacturing of Breathable Superhydrophobic Membranes. *Small Methods* **2024**, *8*, 2400038. [CrossRef]
119. Tan, M.; Gong, R.; Chen, Y.; Kim, M.; Lu, X.; Liu, H.; Yang, R.; Xu, Y.; Zhong, H.; Huang, Y.; et al. Scalable Laser Manufacturing of High-Aspect-Ratio Superhydrophobic and Ferromagnetic Microcilia Arrays for Aqueous Droplet Transportation. *Small Methods* **2025**, *9*, 2500500. [CrossRef]

Disclaimer/Publisher's Note: The statements, opinions and data contained in all publications are solely those of the individual author(s) and contributor(s) and not of MDPI and/or the editor(s). MDPI and/or the editor(s) disclaim responsibility for any injury to people or property resulting from any ideas, methods, instructions or products referred to in the content.